Mafalda Gonçalves Oliveira

Bachelor of Science in Biomedical Engineering

Bacteriorhodopsin monolayers for medical applications: self-assembly and characterization

Dissertation for Master degree obtention in Biomedical Engineering

Supervisors: Prof. Dr. Ana Gomes Silva, FCT-UNL

Prof. Dr. Peter Fojan, Aalborg University

Jury:

President: Prof. Doctor José Luís Constantino Ferreira

Arguer: Doctor Maria Adelaide Miranda

Vowel: Prof. Doctor Ana Gomes Silva

FACULDADE DE CIÊNCIAS E TECNOLOGIA
UNIVERSIDADE NOVA DE LISBOA

June 2017

"Bacteriorhodopsin monolayers for medical applications: self-assembly and characterization"

Acknowledgments

Any kind of cognitive effort reflected in this work is fully dedicated to Professor Ana Gomes Silva for I understand that, for her, it conveys the most pure form of appreciation for support, which was *tremendous* in many dimensions. Growing up is a violent process yet having people worth looking up to by your side makes violence turn into knowledge. I have gained a great amount of knowledge in the last years, provided by Professor Ana's nurturing, highly rational and tactful condition. I thank her for the bottom of my heart for never giving up on me and for the very pleasurable times we had discussing all the scientific issues that arose along this work.

I thank my parents for the patience in standing by me throughout this effort, never having denied me anything from tuitions to a homemade meal that sometimes is so badly missed or a ride to university. Support can be a ghost and I love that ghost. I thank Lola, for accompanying me in my stay in Aalborg with such a patient, attentive, respectful, loving and joyful presence, never ceasing to leave me in awe for how profoundly a dog can teach you about humanity.

I thank Francisco Brasil for the amazing companionship and friendship we had the chance to create in a chaotic time of our lives. I thank all my friends who believe in my capabilities for pushing me light-heartedly through this endeavour and for sustaining the hardship of listening to me yapping on scientific matters.

I also wish to thank Leonid, Eddy and all the staff in the Physics department in Aalborg University for the support and Prof. Kjeld Pedersen and Peter Fojan for the opportunity of working with them.

Abstract

Manipulating bacteriorhodopsin (bR) into a monolayer form has become of growing interest for inclusion in nanodevices for medical purposes such as artificial retina development, mammogram processing optimization and neural silencing. The efficient photoconverting protein's thermal and chemical stabilities are such that bR has become an attractive candidate for protein-based nanostructures, as opposed to other biomolecules. In this type of molecular-scale manipulation, assembling monolayers with high degree of orientation and protein functionality preservation are of paramount importance.

The present work focuses on covalent attachment of 247Cys bR mutant monolayers to a strategically engineered gold substrate through self-assembly process. Covalent attachment of bR in its native form, or purple membrane (PM), on engineered mica substrate is also achieved. Liquid sample characterization via absorption, circular dichroism and steady-state fluorescence spectroscopies is performed as well as absorption spectroscopy on bR deposited on gold substrate and AFM topographic studies on both substrates.

Keywords: bacteriorhodopsin, monolayer self-assembly, protein optical characterization, biomedical nanodevices.

Resumo

Manipular bacteriorodopsina de forma a obter uma monocamada tornou-se um crescente interesse para a sua inclusão em nanodispositivos com aplicabilidade médica tais como retinas artificiais, filtros para optimização de processamento de mamograma e silenciamento neuronal. As estabilidades térmica e química desta efeciente proteina foto-conversora são tais que a bR tornou-se um candidato atraente para nanoestruturas baseadas em proteínas, em oposição a outro tipo de biomoléculas. Neste tipo de manipulação à escala molecular, montar monocamadas com alto grau de orientação e preservação de funcionalidade proteica é de grande importância.

O presente trabalho foca-se em ligar covalentemente monocamadas de mutante 247Cys bR em substratos de ouro estrategicamente funcionalizados através do processo de auto-montagem. Acoplamento covalente de bR na sua forma nativa, ou membrana roxa, em substratos de mica funcionalizados também é explorado. Caracterização da solução líquida através de espectroscopias de absorção, dicroísmo circular e fluorescencia também são realizados assim como espectroscopia de absorção de bR depositada em substrato de ouro e recolha de imagens AFM em ambos os substratos.

Palavras-Chave: bacteriorhodopsina, auto-montagem de monocamadas, caracterização óptica de proteínas, nanodispositivos médicos.

Preface

The main interest of this study is to understand how to manipulate and grow an oriented thin film of this bacteriorhodopsin and to analyse its optical properties keeping in mind its medical applications in the field of biomedical engineering. The experimental work was carried out at the Department of Physics and Nanotechnology at Aalborg University, Denmark, in the spring semester of 2015. The thesis work and writing was developed under the supervision of Professor Ana Gomes Silva, from Faculdade de Ciências e Tecnologia, Universidade Nova de Lisboa and Professor Peter Fojan, from the Department of Physics and Nanotechnology at Aalborg University.

Contents

List of Figures

List of Tables

Glossary

bR	Bacteriorhodopsin
ATP	Adenosine triphosphate
PM	Purple Membrane
SHG	Second Harmonic Generation
CD	Circular Dichroism
AFM	Atomic Force Microscopy
EPS	Electrophoretic Sedimentation
LB	Langmuir-Blodgett
GDP	Guanosine Diphosphate
GTP	Guanosine Triphosphate
ESR	Electron Spin Rsonance
FTIR	Fourier Transform Infrared Spectroscopy
NMR	Nuclear Magnetic Resonance
FS	Fluorescent State
FC	Franck Condon
EFS	Electric Field Sedimentation
Cys	Cysteine
APTES	(3-aminopropyl)triethoxysilane
SAM	Self-Assembled Monolayer
PMT	Photomultiplier

NRMSD	Normalized Residual Mean Square Deviation
MRW	Mean Residue Weight
FWHM	Full Width Half Maximum
XPS	X-ray Photoelectron Spectroscopy

1 Introduction

Since an early age our parents and grandparents feed us with the notion that carrots are good for our eyes, in an attempt to be accessibly fed said carrots. Although the diffusion of this piece of common wisdom may have its roots in a British Intelligence scam in WWII, there is actually some truth behind it.

Behind the complex process of eyesight lies the activation of photoreceptor cells present in the retina, which prompts a biochemical cascade culminating in an electric signal being conducted through the optic nerve into the brain for further processing. The molecular agent of phototransduction in those cells – the rods – is rhodopsin, a protein whose chromophoric group is retinal, or more commonly known, vitamin A (which carrots are rich in – you can thank your mother later). Pathologies interfering in these primary molecular steps of photoreception eventually lead to blindness as in macular degeneration and retinitis pigmentosa.

Such biological entities would soon enough get attention from the scientific community as they consist of a bioelectronic circuit element in which light is converted into an electrical signal, i.e. a naturally occurring phototransducer. In an age where the endeavour for better nanotechnological techniques is growing - as conventional lithography methods reach their performance limit and industry demands are higher and stricter – the attention effortlessly shifts to those functional nano-machines Nature single-handedly crafted and we are now able to include and mimic their design to our convenience. One can make such a bold point as to state that Nature is proof-of-concept for the bare concept of bionanotechnology. There is also an environmental and economic motivation in replacing silicon-based technology for organic and cheaper materials, which bring their own issues especially in terms of stability and degradation and so, optimization becomes a priority.

One of the simplest rhodopsin analogues is bacteriorhodopsin, a microbial rhodopsin responsible for ATP production in extremophile Halobacteria, and its study enables the dynamic modelling and thus better understanding of this and other groups of proteins, as membrane transporters and the pervasive transporters that control neurotransmitter levels in the brain. [1]. Due to the protein's stability in harsh thermal and photochemical conditions and a cyclicity (number of photocyles in lifetime) of about 10^6 with no loss of photonic properties, bacteriorhodopsin has contributed to drop the fragility stigma associated to bio-molecules for inclusion in electronic devices [2]. These features allow one to identify and design several potential bioelectronic applications aimed to optimize, interface, integrate, or substitute the silicon-based microelectronics systems, as well as to develop molecular devices [3].

After its uncertain discovery in 1967 [4], one of the first technical applications and studies for bR was in the form of an ultra-fast photodetector layer [5] and creating layers of bR and capturing/conducting its generated photocurrent has since been a clear scientific effort [6]. Manipulating bR into an oriented monolayer system and appropriate mutation of the protein's amino-acid sequence brought attractive outlooks for applications in the medical sciences, for both major features of this molecule: photochromic and photoelectric. Either feature demands a structural orientation degree of the molecules, but higher orientation is required for photoelectric applications since counter-oriented bR molecules will cancel out each other's photoelectric effect [7] [8].

Layered-bR nanodevices have been proposed as tools for rapid control of cell excitability, i.e. neural silencers, achieving near-100% silencing in rats [9], with prospects of addressing pathologies such as epilepsy and Parkinson's disease [10]. Proposed artificial retinas for retinal degenerative disease patients mimic the light-absorbing capabilities of the homologous native visual rhodopsin and, through the integrated bR film, generates a unidirectional proton gradient that is sufficient to stimulate the remaining healthy neural network of the damaged retina [11][12]. Vision motion detection was also achieved in 2008 with resource to a bR-based photoreceptor array with further artificial vision applications in sight [13]. Also, due to photoinduced isomerization features and associated photochemistry in bR films that lead to photochromic behaviour, their inclusion in Fourier holographic gratings has allowed real-time detection of microcalcifications in mammogram processing, with enhanced resolution and sensitivity [14], [15] . Layered-bR applications extend further from the clinical area, to solar cell sensitizing, optical memories, nanosensing, second-harmonic generation, hydrogen production and biodefense [16][17]. An extensive list of filed patents regarding bR applications (whether layered or not) from various scientific areas can be accessed in the reference section [8], [18].

Similar works to this have been performed with the prospect of technical applications with resort to many different film production approaches, of mono or multi layer configuration. Electrophoretic sedimentation (EPS), Langmuir–Blodgett (LB), polymer embedment and anti-body mediated techniques are described in literature and hold orientation limits, what for photoelectric purposes stands as a challenge. Self-assembly methods provide high orientation and have been applied to bR layer growth purposes, whether for different substrate deposition or for different bR mutants [19]. Covalent anchoring of 247Cys mutant on gold and of purple membrane (PM) on mica is the focus of the present work, with bacteriorhodopsin functionality retention and high degree of orientation.

1.1 Motivation

Among the several interesting applications of this protein, the work developed in this thesis aims to enhance bR's generated photocurrent and optimize its integration in photoelectric systems designed for biomedical applications. The proposed approach lies in the self-assembly of an immobilized, functional, highly-oriented bR monolayer and this is achieved by engineering a mutant bR monolayer that brings the most responsive part of the protein in proximity to the conductive medium through covalent attachment, mediated by a surface linker for native functionality preservation

The manipulation and optical characterization of bR 247Cys mutant for monolayer deposition on gold substrate through the process of self-assembly, as well as of PM on mica substrate, suited for medical photoelectric applications and for second harmonic generation (SHG) studies, respectively. Protein solution quality is assessed via spectroscopic methods such as circular dichroism (CD), absorption and steady state fluorescence spectroscopies, whose results are addressed regarding photocycle dynamics. Absorption spectroscopy of dry bR 247Cys deposited on gold is also discussed as well as atomic force microscopy (AFM) topographic studies for depositions on both substrates.

Through this work, the author also intends to extend personal basic knowledge of molecular scale protein manipulation and characterization for further research in the area of bionanotechnology, to bring the local institution awareness about these versatile biomolecules and to question bio-scaled entities from the physics and engineering paradigms. This way, hopefully bR and other interesting molecules will have their capabilities enhanced and purposely integrated in current biomedical research by means of nanoscaled Nature mimicry.

2

Eyesight, rhodopsin and bacteriorhodopsin

The visual photoreception cascade is briefly introduced with special emphasis on rod photo-biochemistry, where the dynamics of visual pigment rhodopsin engage further neural activity for image processing. Rhodopsin is a 348-long amino acid residue chain consisting of an apoprotein opsin with a central retinal chromophore, responsible for photon absorption at 505 nm. Disturbing rhodopsin's dynamic molecular mechanism results in pathologies such as retinitis pigmentosa, the leading cause of inherited blindness, which is being addressed by biomedical engineering through integration of external and internal electronic implants.

Rhodopsin's analogue, bacteriorhodopsin (whose molecular photo-dynamics resembles that of rhodopsin,) is structurally and functionally presented. A discussion regarding its photocycle dynamics and intermediate states follows, exhibiting its electronic state model from an engineering point of view and pointing current and possible medical applications for bR-based devices.

2.1 Rhodopsin and the visual photoreceptor mechanism

Conscious visual images are set up by the eye's components complex operation. They basically consist of a protective casing, a layer of photoreceptors, a lens system that focuses light on those receptors and a nerve cell system that is responsible for impulse conduction from the receptors to the brain.

The cells responsible for photon reception are the rods and cones (Figure 1b), whose hyperpolarizing (inhibition) potential assumes different shapes. Also, on the one hand, rods are much more sensitive and their level of response is proportional to illumination intensity at levels bellow the threshold for cones. On the other hand, cone response is proportional to stimulus intensity in high levels at which rod response is maximum and fixed. For these reasons cones generate good responses to changes in light intensity but do not represent absolute illumination whereas rods do.

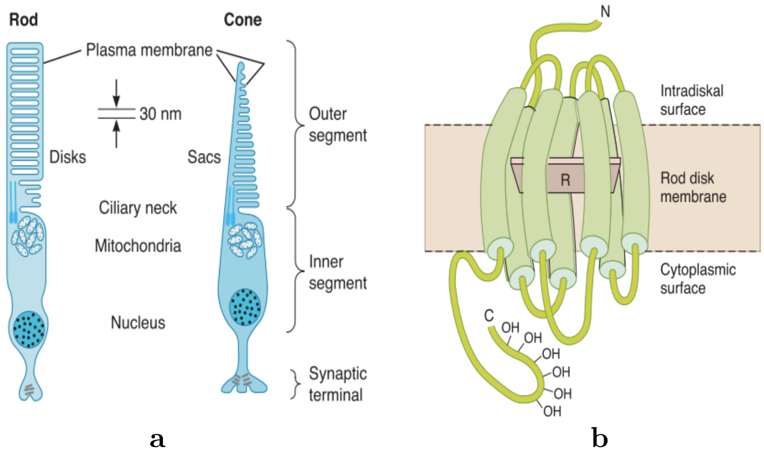

Figure 2.1 – a) Photoreceptor cells in the human eye; b) In the rods one can find stacked disk-like structures with transmembrane photosensitive compound rhodopsin (also called visual purple due to its natural tint), composed of an opsin (represented in green) attached to a retinal through a lysine residue at position 296, parallel to the membrane surface. Rhodopsin's carboxylic acid terminus faces the cytoplasmic side and amino group the extracellular side.

The cascade of events that lead to hyperpolarization or switching-off of the rod synaptic terminal is prompted by conformational changes rhodopsin (Figure 2.1b) suffers due to the isomerization of the retinal chromophore that exists in the 11-*cis* form when in the dark, and absorption of a single photon causes its structure to change to all-*trans* isomer. This isomerization alters the opsin's configuration, translocating a proton across the membrane and leading to activation of the coupled G protein that exchanges GDP for GTP, causing Na^+ channels to close and producing the hyperpolarization potential due to ongoing flux of K^+ (resting potential of -40 mV in these cells is given by the equilibrium of inward ungated potassium – which alone produces a polarization of 70 mV – and inward gated sodium).

2.1.1 **Retinal pathologies**

Unsurprisingly, vitamin A deficiencies will produce visual abnormalities. The first to manifest will be nyctalopia or night blindness, followed by xerophtalmia – damage in the cornea and retina which eventually lead to blindness. Rods function is altered but concomitant cone degeneration also occurs as the vitamin deficiency develops. Prolonged deficiency is associated to anatomical changes in the rods and cones followed by degeneration of the neural layers of the retina. Restoring vitamin A levels also restores retinal function if given before the destruction of receptors [20].

Retinal diseases, though, have a large contribution from rhodopsin mutations. The mainly studied pathology is retinitis pigmentosa, a hereditary degenerative disease, which at least 1.5 million people suffered from in 2012. More than 150 mutations on the opsin gene are reported but some of them may not even interfere in the precise molecular mechanism involved in rhodopsin photoreception, unlike others which result in misfolding conditions (derived from formation of non-native disulphide bonds between helices), opsin mislocalization, altered stability/function and c-terminus truncation [21].

Since around 20 years ago, scientists have been making efforts in order to replace degenerated photoreceptors with electronic devices initially consisting of a silicon-based photodiode arrangement powered only by natural light, whose excitation upon small amount of light was not enough to restore visual perception. Nowadays, 'active' electronic amplification is achieved with a subretinal photodiode implant that addresses individual pixels excited by near-infrared-emitting goggles [22], much like a subretinal hexagon-lattice solar cell (Figure 2.2) designed to mimic rhodopsin's trimeric tertiary structure.

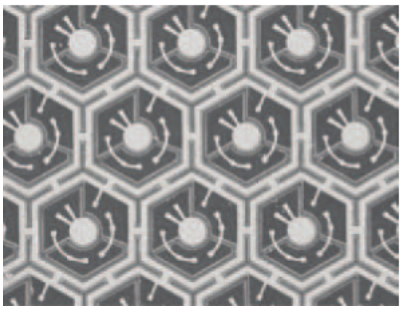

Figure 2.2 – Triple-photodiode array device for subretinal stimulation, developed in 2012 by Mathieson et. al., mimicking rhodopsin's trimeric conformation naturally presented through the rod disk membrane. Disposed over an area of 70 μm^2 it produces a voltage of 1.5 V upon photon excitation in the 880-905 nm range.

2.2 Bacteriorhodopsin

Rhodopsins belong to the family of G-coupled seven-transmembrane helix proteins and divide in two main categories – microbial (where bacteriorhodopsin is included) and visual. Although the form and functions displayed are diverse, they are all characterized by a retinal chromophore attached to an opsin and for the isomerization cycle that takes place upon light absorption.

Bacteriorhodopsin's structure and function highly resembles those of visual rhodopsins [23] and interestingly enough, they evolved independently. Their three-dimensional quaternary structure is also analogous, where each trimer is composed monomers disposed in a 2D hexagonal crystal lattice.

Due to bR's simplicity and stability, high quantum efficiency (0.64) and to the fact that bR is enhanced in the native transmembrane conformation, it has long served as the prototype for elucidating general features of vectorial transport across a cell membrane [24]. Furthermore, most of previous pharmaceutical studies aiming at G-coupled proteins (such as visual rhodopsin) were based on the structure of bR and it still remains an important model for such studies [25].

Figure 2.3 – Koyashskoe Salt Lake in the Crimean peninsula is one of the bodies of water that, due to *halobacteria* proliferation and consequent bacteriorhodopsin content, is purple-tinted. (Photo: helena2010/Shutterstock)

Bacterial extremophiles *Halobacterium halobium* (from greek *hals*, salt) which thrive in extreme salinity conditions up to 6 times that of salt water, when in oxygen deprivation, maximize bR expression in its membrane and switching from respiration to photosynthesis [26] for ATP synthesis. The protein acts like a light-driven proton pump, absorbing a photon and prompting a number of protonation/deprotonation reactions and proton exchange with the aqueous phase on both sides of the membrane, culminating in ADP phosphorylation [27]. Its purple hue paints salt lakes around the world, in an exotically nature-crafted landscape as the one represented in Figure 3.1.

Curiously, if we examine from an evolutionary point of view the absorption spectra of the parallel photosynthetic system chlorophyll and overlap it with bacteriorhodopsin's, one notices the former may have developed to take up wavelengths not absorbed by the latter, suggesting that earliest aquatic bacteria expressing a rhodopsin-like system developed in a higher strata than of chlorophyll systems.

2.2.1 Structure and retinal environment

The 248 amino-acid sequences of 26 kDa which composes bacteriorhodopsin folds into a seven-transmembrane helix topology (A to G) with short interhelical loops, spanning the lipid bilayer and forming a transmembrane pore mainly between helices B, C, F, and G as depicted in Figure 2.4 where key residues in proton translocation are identified.

The linear retinal chromophore locates itself in the internal protein pocket and is bound at about a 20° angle (in relation to the membrane plane) to the Lys216 residue in helix G through the nitrogen atom of a protonated Schiff base, which interrupts the pore and separates an extracellular half channel from a cytoplasmic half channel [28][29]. The retinal side chain in the binding pocket is closely packed between four tryptophan residues, and the positively charged Schiff base interacts electrostatically with the opsin environment [7].

As for quaternary structure, and as mentioned earlier regarding both bR and visual rhodopsin, bR monomers organize within the plasma membrane and across its 6 nm of height as a two-dimensional, hexagonal crystalline lattice of uniformly oriented homo trimers, referred to as the purple membrane (PM) or native bR [19]. The trimers are mostly stabilized through crystallographic lipids.

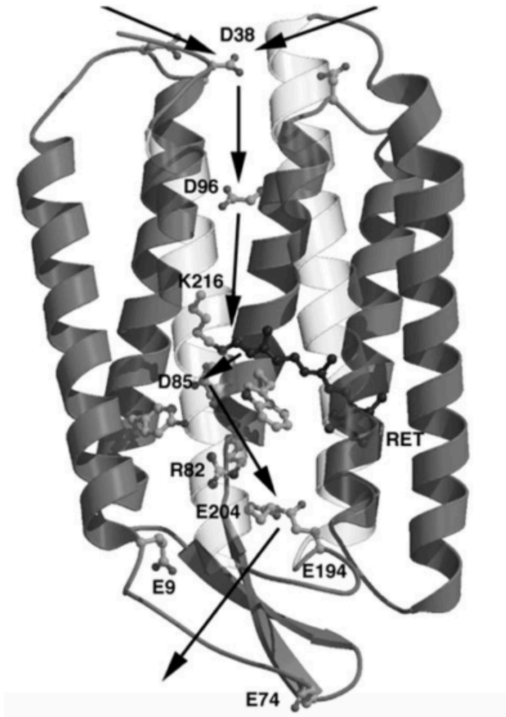

Figure 2.4 – Bacteriorhodopsin monomer with important residues in proton translocation. Seven transmembrane alpha-helices surround a central retinal chromophore whose photo-excitation induces deprotonation of the Schiff-base leading to conformational changes in the opsin. Height in membrane of 6 nm; carboxylic terminus (top) more negatively charged than amino terminus (bottom) i.e. cytoplasmic side more negative in relation to extracellular side.

2.2.2 bR photocycle and retinal electronic state model

Upon photon absorption, the all-*trans* retinal (only isomer in light adapted-bR and mixed in a 1:1 ratio with 13-*cis* isomer in dark-adapted bR) chromophore isomerizes to its 13-*cis* form and prompts bR conversion from its ground state bR_{568} to a series of photo intermediates, following through a photocycle presented and discussed in Figure 2.5. This rapid isomerization of retinal in combination with well-defined conformational changes in bR during the photocycle leads to the transport of a proton from the cytoplasmic to the extracellular side of the membrane.

Each intermediate has a distinct absorbance maximum and lifetime, and are commonly represented by a single letter code where the index represents the absorption maximum. Interestingly, all the intermediate states can be photochemically switched back to the ground bR_{568} state by absorption at a wavelength that corresponds to the maximum of the respective intermediate [16].

$$\mathrm{bR}_{570} \xrightarrow{h\nu} [\mathrm{S}_1^{\mathrm{FC}}(\mathrm{H}), I_{460}, J_{625}] \xrightarrow{3\ \mathrm{ps}} \mathrm{K}_{610} \xrightarrow{2\ \mu\mathrm{s}}$$
$$\mathrm{L}_{550} \overset{50\ \mu\mathrm{s}}{\rightleftarrows} \mathrm{M}_{412} \overset{2\ \mathrm{ms}}{\rightleftarrows} (\mathrm{N}_{540}, \mathrm{O}_{640}) \xrightarrow{8\ \mathrm{ms}} \mathrm{bR}_{570}$$

Figure 2.5 – bR photocycle; when exposed to green light, the molecules in the ground state (bR_{568}) convert to short-living J_{625} and proceed to the K_{590} state. This photoreaction initiates a cyclic sequence of thermal conversions (L_{550}, M_{412}, N_{540}, and O_{640}), which finally lead back to the bR_{568} state. In dry conditions later N_{560} and O_{640} intermediates are no longer observed, only the K_{590}, L_{550}, and M_{412} intermediates of the dry bR are involved in the photochemical cycle [30].

The photoinduced conformational changes through the bR photocycle have been extensively studied using a wide range of time-resolved electron spin resonance (ESR), atomic force microscopy (AFM), FTIR, ultrafast laser spectroscopy) and steady-state spectroscopic methods (X-ray diffraction, NMR, electron microscopy). Isomerization steps from all-*trans* to 13-*cis* conformation along torsion of retinal's $C_{13}{=}C_{14}$ bond (Figure 2.6) are tentatively described by the two-state electronic model presented in Figure 2.7 [31] although other models have been more recently proposed.

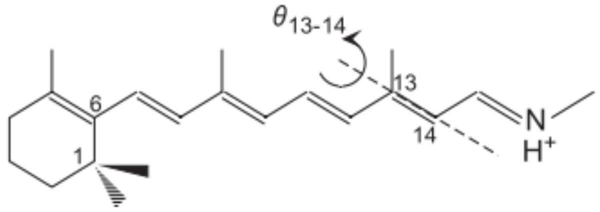

Figure 2.6 – Retinal structure with represented torsional axis and coordinate C_{13}-C_{14} double bond where photoinduced isomerization occurs.

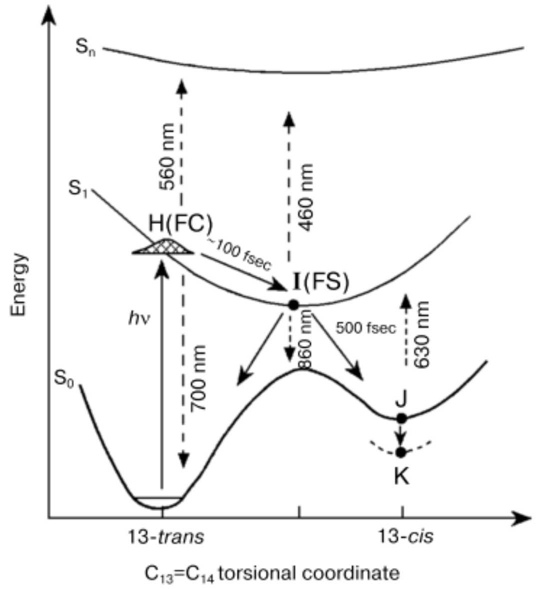

Figure 2.7 – Electronic two-state model of primary events of retinal after light-induced excitation. Upon excitation, the generated wave packet is driven out of the Frank-Condon region through non-radiative vibrational relaxation. Electronic relaxation occurs at mid-isomerization. More recent models discuss the point at which reactive vs non-reactive branching occurs, suggesting it is prior to S_1-S_0 transition as represented.

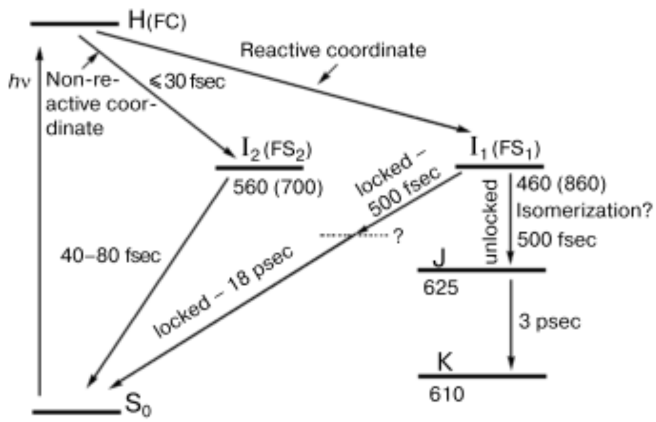

Figure 2.8 – Electronic structure of primary events in bR. Existence of two fluorescent states FS_1 and FS_2 dictates whether bR remains in its photocycle by stimulated fluorescent emission at 860 nm to J_{625} intermediate, or relaxes back to its ground state without complete retinal isomerization into 13-*cis* geometry.

However, recent time-resolved femtosecond studies in C13=C14 locked bR have suggested that the FC (and not FS) state in native bR branches into two molecular pathways: reactive (isomerization) and non-reactive (back-reaction), going forward along the photocycle or leading back to the relaxed all-*trans* ground state, respectively, as shown in the diagram in Figure 2.7 [32].

bR's high quantum efficiency of 0.64, is directly related to the probability of the reactive electronic pathway being followed. Stimulated emission at 860 nm is interpreted to reflect the wave packet motions in the reactive excited state, relaxing electronically to the next photo-intermediate, J_{625} [31].

3

Oriented bR Monolayer Self-Assembly

The ability of bR to form two-dimensional thin films with excellent electro-optical properties and high thermal (up to 80° C), mechanical and chemical robustness encourages its use in biophotonic devices (including artificial retina implant) for photocurrent generation – a single layer of PM can generate up to 300 mV upon excitation but device integration is a more delicate task since efficient interfacing with electron conducting metal electrodes stands as a difficulty [8]. Efficient interfacing comprises the fulfilment of the following challenging factors:

(1) Stable immobilization;

(2) Preferential unidirectional orientation;

(3) Preservation of bR's functionality.

The proper approach resides in producing oriented bR layers for which various methods are described. Depending on the projected application, parameters as thickness, coverage and orientation degree may vary and for photoelectric purposes the degree of orientation is the crucial point [8] since electron pathways must not cancel out [3].

bR layers are most commonly deposited using the Langmuir-Blodgett (LB) technique that yields thin layers but possible random orientation [30] and electric field sedimentation (EFS) - where a dipole moment directed from the cytoplasmic side to the extracellular side is generated – but with difficulty in obtaining ultrathin films of well-defined surface density, coverage and thickness for reliable current transport due to large size of PM patches that form and their tendency to aggregate and stack. A high degree of orientation is also compromised since both termini are negatively charged with small measurable difference (carboxylic more negative), making it nearly impossible to properly specify the protein orientation through an electric field and merely achieving a preorientation that has to be made permanent for example by covalently anchoring bR on the desired substrate [7]30,33].

Moreover, and well-illustrated below in Figure 3.1, delipidating bR from its crystallographic lipids results in a 300% increase in generated photocurrent density, due to increased functional molecular density. Delipidation in PM occurs with retention of photoelectric properties, releases the protein trimers from rigid two-dimensional patches, and facilitates a stable, densely packed chemisorption when in the presence of a favoured connection site, like an anchoring cysteine residue on a gold substrate [19]. PM's patched quaternary structure brings strong physisorption to substrate through high contact area and stabilizes bR's photocycle, bringing interest in for optimizing isolated trimeric bR applications.

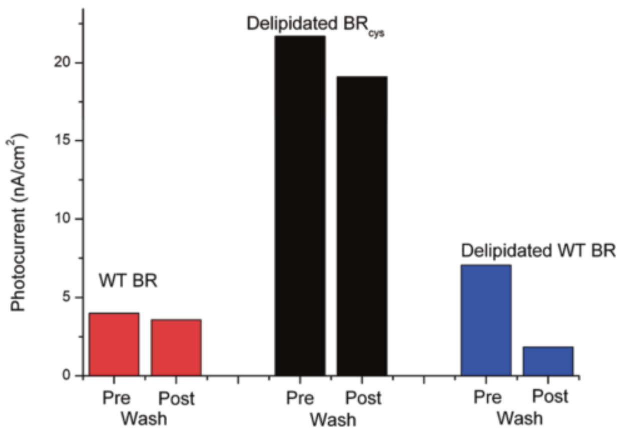

Figure 3.1 – Photocurrent measurements and stability before and after salt/surfactant wash in wild-type bR, delipidated wild-type bR and delipidated bR cys mutant samples.

The fact that metallic substrates as gold allow ballistic electron conduction and heat dissipation while being chemically inert (valuable for biomedical applications due to biocompatibility concerns), and mica substrates allow bacteriorhodopsin second-harmonic generation studies due to its null signal in this non-linear optical spectroscopy, interest in appropriately attaching bR to these substrates arose. Strategic connection sites are engineered and this work will focus on the perpendicular self-assembly of the 247Cys bR mutant covalently attached to gold, and native purple membrane covalently attached mica substrates.

3.1 247Cys bR chemisorption on gold

Replacing a native threonine residue for a highly responsive cysteine (Cys) residue on the carboxylic terminus at position 247 of bR's amino-acid sequence provides prospects for gold covalent attachment – the strongest chemical bond - at favourable unidirectional orientation [34], represented in Figure 3.2 for a mutant of the same family.

Cysteine is a thiol whose functional group, sulfhydryl (SH), suffers deprotonation, leading to thiolate-Au binding with strength close to that of Au-Au bonds. This strategy elegantly tackles the unstable preorientation issue discussed above that compromises effective electrode interface. Cysteine's SH terminal is also capable of forming or S-S (disulphide) bonds with other Cys bR molecules (interprotein) or with a thiol surface linker monolayer.

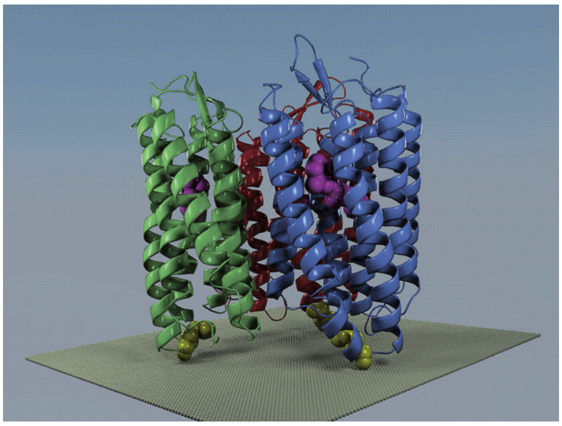

Figure 3.2 – The 163C mutation on the E-F loop of bR has been designed to exploit the possibility of bringing the most responsive part of the protein into close proximity to the underlying surface - a gold electrode – through triple point chemisorption (yellow), one for each monomer in the trimer. The developed layer for enhanced photoelectric application has reported a 20% increase in generated in photocurrent densities in relation to native also delipidated PM.

High proximity from bR to gold electrode via mutant cysteine (3Å) should promote direct electron transfer (via Auger-mediated de-excitation in the Au layer) leading to higher photocurrents but an increase is reported upon addition of a surface linker that mediates electron transfer. It has been suggested that due to gold's known unspecific binding affinity to proteins, unspecific attachment would compete with cysteine-mediated attachment, lowering the surface coverage of preferentially oriented bR and consequently, generated photocurrent [35]. Also, bR conformation upon immobilization and limited access from reactants to our protein's active site might be compromising bR's functionality.

Self-assembling a dithiol (as the one depicted in Figure 3.3) monolayer on the gold surface with its SH group exposed at the SAM-air interface, allows bR to spontaneous and uncatalytically attach to the surface through disulphide bonding with its cysteine residue [36]. Although approximately 20% of adsorbed 1,6-hexanedithiol forms loops through S-S bonding after the SH terminals suffer ambient oxidation (minimized due to short length of the carbon chain), the remainder will provide precise immobilization of bR while preserving its native functionality and providing improved electron transfer to the electrode [37].

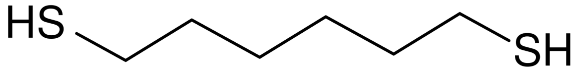

Figure 3.3 – 1,6-hexanedithiol SAM deposited on Au results in a height of approximately 12.3 Å [38].

3.2 Purple membrane chemisorption on mica

Second-order non-linear optical phenomena are very sensitive to chirality. The interactions driving the surface orientation on PM's 2D quasi-crystal structure leads to a high second-harmonic generation (SHG) response, making it possible to probe chiral geometry in bR ultrathin films and consequently, provide orientational studies. Therefore, surface orientation studies on mica were also carried out are useful for comparison to attachment on metallic substrates.

Atomically flat mica substrates allow SHG studies on deposited bR since no signal will result from the substrate, isolating the signal derived exclusively from the deposited material. Yet, bR's negative extremities poorly adsorb to mica and with no preferential orientation due similar electronegativity in both termini. The first step is then to find conditions where the membrane layers are adsorbed in the substrate.

Aminosilanizing mica will lead to a positive surface charge caused by its terminal amino groups to which PM will bind [39], creating a carboxyl-terminated self-assembled bR monolayer. (3-aminopropyl)triethoxysilane (APTES) monolayer deposition through vapour-phase technique results in 4-5 Å high monolayers with 40° contact angles [40]. Making use of a silanetriol as 3-(mercaptopropyl) triethosxysilane) with SH terminals would provide prospects for covalent attachment to 247Cys bR through disulphide bonding as explained in the earlier section.

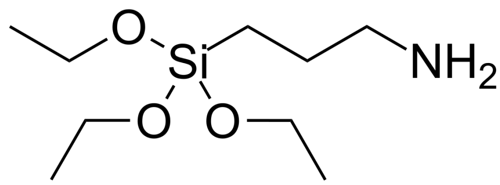

Figure 3.4 – APTES with amino terminus.

4

Experimental Methods

In this section, all experimental procedures are outlined starting with protein sample characterization through linear spectroscopic methods as circular dichroism, absorption and fluorescence emission spectroscopies. Then follows the 247Cys bR monolayer deposition procedure for gold substrate, with and without surface attachment through 1,6-hexanedithiol self-assembled monolayer, and for PM on mica substrates, with and without surface attachment through silane self-assembled monolayer. Finally, topographic studies on AFM on all substrates and absorption spectroscopy for deposition on gold substrate are performed. All experimental parameters, methods and setups are described.

4.1 Optical Characterization Techniques

Circular dichroism spectroscopy allows for secondary structure estimation, in which high alfa helix content would be targeted as a result (protein all folded in solution) meaning the protein was in optimal folding conditions. Absorption spectroscopy enables confirmation of photon absorption by the all-*trans* retinal as well as protein concentration determination, which will dictate how fast the monolayer will form, and we wish to favour assembly over aggregation, so suitable kinetics must be controlled through proper concentration. Fluorescence spectroscopy ensures the protein is following a reactive energetic channel, i.e., undergoes its photocycle. This way, functionality and proper immobilization probabilities are maximized.

4.1.1 Absorption Spectroscopy of liquid phase bR and of 247Cys bR on Au

Absorption spectroscopy on liquid samples allows for determination of sample molar density, c, through the absorbance, A, and using the Beer-Lambert's Law (1). The absorbance depends on molar attenuation coefficient in $\mathrm{M^{-1}cm^{-1}}$ ε_M, the optical path, l, upon measurement i.e. the cuvette's optical path, in cm, and sample molar density c

$$I = I_0 10^{-\varepsilon_M c l} \tag{1}$$

$$A = -\log\frac{I}{I_0} = \varepsilon_M c l \tag{2}$$

$$\mathrm{A} = 2 - \log(T\%). \tag{3}$$

The above equation relates absorbance with the measured transmittance, with the transmittance defined as

$$\mathrm{T} = \frac{I}{I_0} \tag{4}$$

$$A = \varepsilon_M c l \tag{5}$$

$$c = \frac{A_{568}}{\varepsilon_{M,568} l} \tag{6}$$

As the attenuation coefficient is a function of λ, so will the absorbance depend on wavelength and so, for molar density calculation one must provide required data.

The liquid bR sample was maintained in the same quartz cuvette. The measurements were performed in a Perkin Elmer Lambda 1050 UV/VIS/NIR spectrophotometer, with the PMT, InGaAs and PbS 3D detection module (flushed with N_2) attached in the detection area, in a 200-1800 nm range with a 1 nm interval step in absorption mode. For best bR absorption peak visualization, a 400-800 nm range measurement was also performed. Measurements referenced by deionized water and autozeroed for every measurement. Tungsten Halogen lamp in continuous mode was used as light source 360-2000 nm.

Solid sample absorption characterization allows understanding of size effects upon deposition, evidencing aggregates or a more uniform distribution but in order to obtain a correct transmittance measurement for a solid sample, the possibility of the transmitted beam deviating and diffusing in relation to the incident beam must be taken into account due to scattering. Overall transmittance, i.e. direct transmittance plus diffuse transmittance can only be measured using a specific item of equipment known as an integrating sphere. With resource to one in the detection module, scattered light is also collected and accounted with.

The measurements were performed in a Perkin Elmer Lambda 1050 UV/VIS/NIR spectrophotometer, in transmission mode in the 400-800 nm range, with and integrating sphere in the detection module, for the study of solid samples as discussed above. Absorption spectra in the NIR/VIS range (nm) for 247Cys bR on bare gold and on thiolized gold were recorded. The bare gold spectrum was also recorded.

4.1.2 Fluorescence Emission Spectroscopy

Fluorescence is an electronic radiative relaxation process to the ground state S_0. The molecular agent that fluoresces after excitation is referred to as a fluorophore.

The fluorophore remains in the lowest vibrational level of the excited electronic state for a period on the order of nanoseconds, the fluorescence lifetime. Fluorescence emission occurs as the fluorophore decay from the singlet electronic excited states to an allowable vibrational level in the electronic ground state. Detecting photon resulting from fluorescent emission allows for electronic state studies of a sample of interest.

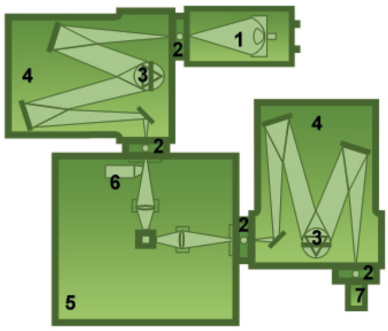

Figure 4.1 – Typical experimental setup for steady-state fluorescence emission spectroscopy. 1-Broadband light source; 2-Filter; 3-Grating; 4- Monochromator; 5 -Sample compartment 6-Excitation corrector; 7- Detector; QuantaMaster 300.

The sample was moved into a suitable fluoroscopy cuvette and the steady-state emission scan performed on a PTI QuantaMaster 300 Spectrofluorometer with a high power (75 W) Xenon flash lamp. Experimental setup was analogous to that represented on Figure 4.1. Excitation wavelength corresponds to maximum in previously measured absorption, 568 nm and the emissions were measured in the 630 – 900 nm range, being careful not to allow emission scanning across the excitation wavelength.

4.1.3 Circular Dichroism Spectroscopy

Circular dichroism (CD) is a linear optical phenomenon in which a molecule absorbs right-hand circularly polarized light (RCPL) and left-hand circularly polarized light (LCPL) to different extents. For a molecule to exhibit this optical activity, it must contain a chiral chromophore like retinal. Chirality (from the greek *kheir* that means hand, a very familiar chiral object) is a geometric property of certain isomeric species that are mirror images of one another and yet do not superimpose. The majority of biological molecules are chiral including DNA and RNA, and curious and mysteriously, many only exist in one enantiomeric conformation although both structures have the same formation energy and thus formation probability [41].

CD spectrophotometers detect these variations in absorbance for LCPL and RCPL across a sample. A source of monochromatic linearly polarized light transverses a photoelastic modulator (PMT) generating circular polarized light by a change in the birefringence of the optical element in the PMT, first left and then right, which will be absorbed to different extents by the photoactive sample. A photomultiplier tube detector detects the transmitted light in order to calculate absorbance.

A largely used application for CD spectroscopy is the secondary structure content studies of proteins, each coming across spectroscopically in the far UV (190-250 nm) region with a distinct signature as seen below in figure 4.2.

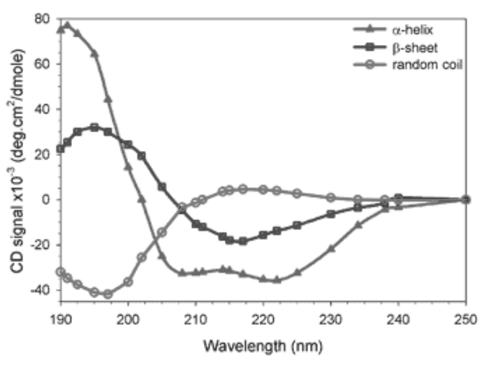

Figure 4.2 – Circular dichroism "fingerprint" for pure alpha helix, beta sheets and unordered structure protein. Leeds University.

The observed spectra for each protein will depend on its alpha-helical, beta-strand and coiled structure content and results from the linear combination of proportion content. Proper secondary structure content allows for sample quality assessment and ensures folding conditions of bacteriorhodopsin are coherent with expected, making sure the protein did not denature.

Circular dichroism can be measured in several units. Literature reports many conflicting units and so below are the conversion equations used. The per residue molar attenuation units of circular dichroism in $M^{-1}cm^{-1}$, $\Delta\varepsilon$, is sometimes referred to as molar circular dichroism.

Machine units measure the difference in molar attenuation coefficients between left and right-handed polarized light, usually between 1 and 100, and need to be corrected to account for the amount of protein used in the sample. To convert from measured machine units in degrees θ_λ to $\Delta\varepsilon$, one must first calculate mean residue ellipticity, $[\theta]_{MRW,\lambda}$, through equation 7 and then introduce the result in equation 9.

$$[\theta]_{MRW,\lambda} = \frac{MRW\ \theta_\lambda}{3298\ l\ c} \tag{7}$$

Where:

$$\text{MRW} = \frac{Molecular\ Weight}{N°Residues - 1} \tag{8}$$

$$\Delta\varepsilon = \frac{[\theta]_{MRW,\lambda}}{3298} \tag{9}$$

The sample was transferred into a quartz cuvette (Hellma Analytics 0.1 mm optical path). Measurements were performed in a Jasco J-1500 CD spectrometer in the 190-400 nm range with a step resolution and band width both of 2 nm, 100 millidegree sensitivity, 5 accumulations and 50 nm/min speed. After the measurements, the sample was kept in a refrigerator.

4.2 **AFM Topography studies**

Atomic force microscopy (AFM) allows for topographic studies of the samples in order to assess surface distribution, density, and height of deposited material in the substrates. Purple membrane on silanized and bare mica was studied as well as 247Cys bR mutant on thiolized and bare gold substrates.

The studies were performed in a NTEGRA Aura Atomic Force Microscope on tapping mode – lessening the damage to the biological sample - with an Olympus OMCL-AC160TS-R3 silicon micro cantilever with aluminium reflex coating with a tip radius of 7 nm. Several AFM topographic images were taken for different samples:

1. PM on bare mica (Figure 5.9)
2. PM on silanized mica (Figure 5.11)
3. Isolated 247Cys bR on bare gold (Figure 5.13)
4. Isolated 247Cys bR on thiolized gold (Figure 5.15)

Images were imported to and analysed in the open source software Gwyddion. Plane levelling and zero-fixing were applied to all raw AFM images. Lateral and vertical dimensions of the adsorbed species can be obtained from the image and from height profiles, respectively.

4.3 bR Monolayer Assembly

bR was deposited on two different substrates both with and without a suitable monolayer responsible for maintaining the protein's orientation and anchoring. A gold substrate should best dissipate heat and conduct generated photocurrent best for photoelectric applications. Muscovite mica substrates should allow optimized second harmonic generation measurements, since due to its intrinsic geometry, will not produce an SHG signal.

4.3.1 PM monolayer assembly on bare mica

Freeze dried purple membrane is diluted in 250 µL of deionized water (Sigma-Aldrich) in an Eppendorf tube and placed in floater in an ultra-sound bath (frequency) for about 10 minutes in order to produce uniform particle size. The suspension is then pippeted onto a freshly cleaved muscovite mica sheet and left to dry in air.

4.3.2 PM monolayer assembly on aminosilanized mica

Mica aminosilanization is achieved through gas-phase deposition and two samples were prepared through the same procedure. A freshly cleaved mica sheet is placed in a petri dish and put inside the apparatus together with 250 µL of silane and 750 µL of toluene (Sigma Aldrich) in Eppendorf tubes. Toluene has a lower boiling point than silane, so it is used as a carrier for silane evaporation. The vacuum system is turned on for about half an hour. The system is then flushed with argon, which at a higher density than air will squeeze it out of the system without reacting with mica. Purple membrane is then diluted in incubation buffer and 250 µL of sample are deposited on the silanized mica sheet and placed in refrigerator.

4.3.3 247Cys bR monolayer assembly on bare Au substrate

The bR suspension was firstly diluted in a freshly prepared suspension buffer (150 mM KCl, 10 mM Tris-HCl) to a final absorbance of 0.242 (ideally between 0.2 and 0.3) at 570 nm and stored in an Ependorf tube.

After 30 minutes in the UV cleaner, a gold chip (Xantec, 0.3 mm thick) was placed in a petri dish. 20 µL of bR in suspension buffer (as described in previous paragraph) and 100 µL of incubation buffer (300 mM KCl, 10 mM Tris-HCl, pH 7.2) were simultaneous and immediately cast onto the centre of the chip, followed by two hours of incubation in a dark and dry environment. The chip was rinsed with no more than 500 µL of incubation buffer, at a 45° angle onto an absorbing surface. It was then placed in a petri dish with deionized water, gently shaken, dried with N_2 and stored in a refrigerator.

4.3.4 **247Cys bR monolayer assembly on thiolized Au substrate**

18 mL of absolute ethanol (Fluka) were degassed for 10 minutes with N_2 and mixed in a 50 mL polypropylene test tube with 9 µL of 1,6-hexanedithiol (Fluka) to a 3×10^{-3} M molar concentration. A previously UV cleaned (for 30 minutes) Au chip was immersed in the solution and the test tube left overnight in a refrigerator, hermetically sealed. Afterwards, the Au chip was carefully removed from the tube, rinsed off with 96% ethanol (Fluka) and gently dried with a N_2 steam without allowing ambient oxidation. The procedure for bR deposition on this system is the same as for plain gold and therefore, the stages were repeated and the chip stored.

5

Results and Discussion

5.1 Circular Dichroism Spectroscopy

Circular dichroism data was analysed online through DichroWeb [42]–[44]. The CD raw data consisted of 105 points in millidegree from 190 nm to 400 nm with a 2 nm step. Since DichroWeb only allows for data input to have a 1 nm step, the data was interpolated and smoothed for the required step.

Secondary structure estimation from CD data was obtained through DICHROWEB with three different analysis methods (SELCON3, CONTIN, CDSSTR) and the appropriate available data sets (from Set4, Set7, SMP180 and SP175 size, type of proteins it contains may not be analogous and result in poor NRMSD). If the sample is totally unknown in terms of structure, each viable reference dataset should be used and the results examined for their NRMSD value. Data sets containing secondary structure of alike proteins related to the one in study yields higher NRMSD. bR's secondary structure is mainly alpha-helical with very low beta-sheet content, as reported in literature and shown in table 2, and conformation similarity to available proteins present in DichroWeb data sets is unsatisfactory, so low NMRSD values as well as poor content estimation are expected.

Mean residue weight was calculated using equation (8).

$$\text{MRW} = \frac{26\ kDa}{247} = 105.26\ Da$$

Raw data in machine units are converted to degrees and introduced in equation 7, along with the optical cuvette light path of $l = 10^{-2}$ cm and the obtained concentration from absorption spectroscopy results, of 3,945 mg/mL.

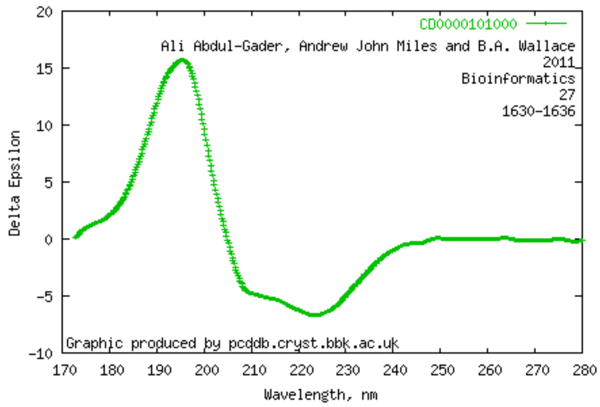

Figure 5.1 – Bacteriorhodopsin circular dichroism spectra from PCDDB in delta epsilon units. [Plotting this data file against measured and converted data, results in good NMRSD].

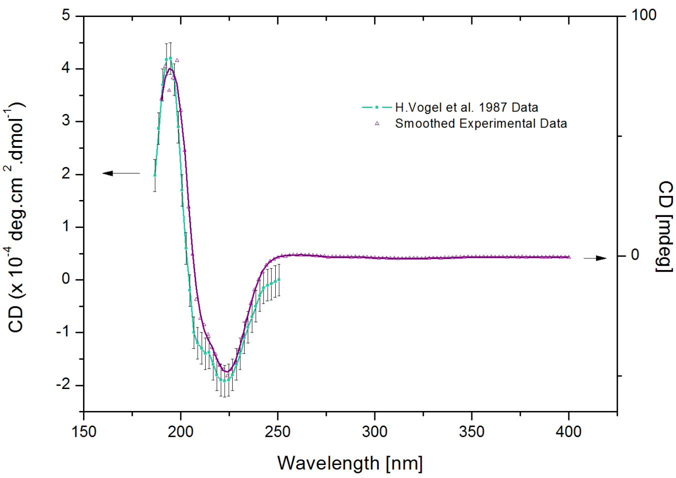

Figure 5.2 – Circular dichroism experimental data for bR suspension against H. Vogel data. Curve shape similarity reveals secondary structure content is approximate.

Plotting measured data against bR's CD data from literature results in better visual elucidation of secondary structure similarities and thus, confirmation of proper folding conditions for deposition. CD data from H. Vogel et. al. allows approximation of alpha-helix content of our sample of 61%.

Table 5.1 - Secondary structure content estimation from circular dichroism spectroscopy data, which yielded the best results from all methods and databases available DichroWeb.

Method	Database	Alpha-helix	Beta-sheet	Unordered	NRMSD
SELCON	Set 7	0.368	0.178	0.468	0.300

Poor and not according to literature results were expected upon available protein data set analysis. Alpha-helical content is too low and beta-sheet is too high. Low NMRSD value confirms poor fitting results.

Since a cysteine residue is accessible for sulphide bonds with the substrate, it is also likely that interprotein disulphide bonds form (Figure 5.3), bringing two bR chains into close contact and compromising bR's helical integrity. Nevertheless, beta-sheet structures cannot have formed, so the excess in this conformation content cannot derive from mutational interference on secondary structure.

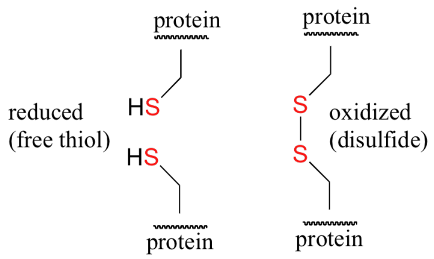

Figure 5.3 – Interprotein disulphide bond.

Table 5.2 - Reported secondary structure from literature

Author	Alpha-helix	Beta-sheet	Other
B. K. Jap et al (1983)	0.52	0.26	-
H. Vogel et al (1987)	0.61	0.18	0.22
B. A. Wallace et al (2011)	0.697	0.48	0.254

5.2 Fluorescence Emission Spectroscopy

The acquired emission spectrum for our liquid 247Cys bR sample is shown below in figure 5.4. It shows a single narrow peak with emission maximum at 857 nm. Relative photon count is low due to the intrinsic isotropic emission of the excitation xenon lamp so only a portion of its power will efficiently excite our sample. Knowing the approximate number of excitation photons allows for calculation of the quantum yield of this transition contributing to characterize the protein's photoelectric efficiency and justify its inclusion in nanotechnological integrations – although this is an interesting analysis, it falls out of the focus of this work.

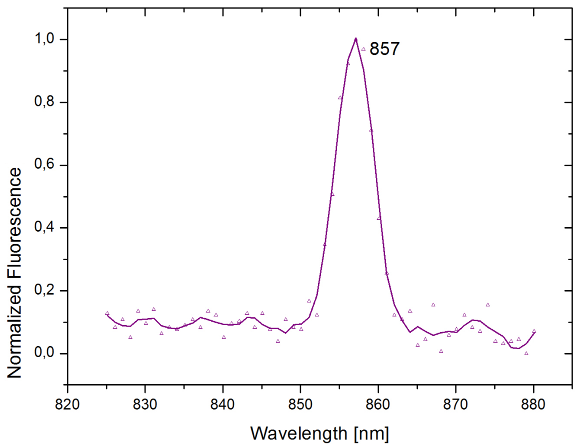

Figure 5.4 – Normalized fluorescence emission data for liquid sample bR.

Taking into account bR's photocycle and retinal's electronic state model diagram in figures 2.7 and 2.8 the measured emission peak corresponds to stimulated emission of the reactive intermediate I_{460} converting to next photocycle intermediate J_{625}. This means that the all-*trans* retinal absorbed a photon which induced its transition to the first excited state S_1, underwent non-radiative vibrational relaxation from the Frank-Condon region (H) towards energetic minimum FS_1, and emitted a 857 nm photon upon transition to its fundamental electronic state and bR followed the reactive pathway via I_{420} intermediate, undergoing the remainder portion of its photocycle via J_{625} intermediate, and back to the ground state bR_{568}. Since the photocycle is completed and the retinal chromophore returned to its all-*trans* conformation, we ensure proper protein functionality before the immobilization stage.

5.3 Absorption Spectroscopy on liquid phase bR

The collected absorbance spectrum for our 247Cys bR liquid sample shown in figure 5.5 reveals a broad peak in the 450-650 nm range, with maximum absorption intensity at 568 nm, in optimal accordance with literature [45]. This implies that bR's retinal chromophore in its fundamental all-*trans* state, S_0, is absorbing light and transitioning to its first electronically excited state, S_1, initiating the isomerization to its 13-*cis* isomer which occurs as bR_{568} is photoinduced into its cycle towards Frank-Condon region and vibrationally relaxing to intermediate state I_{460}. This confirms chromophore is functional and photoactive.

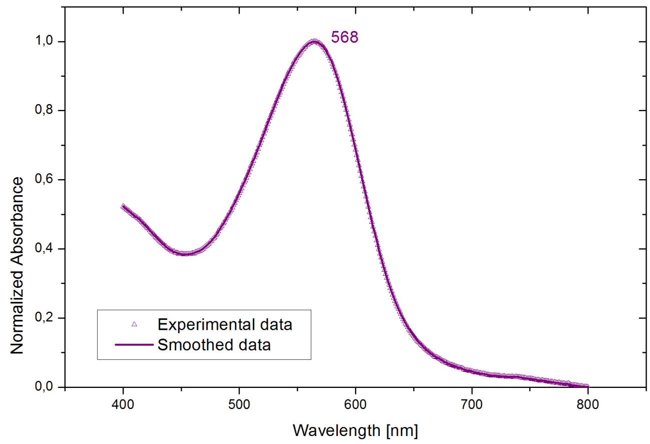

Figure 5.5 – Normalized absorbance measured for 247Cys bR mutant with 1 nm step.

Bacteriorhodopsin liquid suspension concentration for monolayer deposition purposes should fall in the 10-20 µM range in order to guarantee proper deposition kinematics, so that the assembly quickly occurs while aggregation is avoided, which would be favoured for higher concentrations.

Molar attenuation coefficient for bR, at its maxima absorbance, is $\varepsilon_{M,568} = 6{,}3\times10^4\ \mathrm{M^{-1}cm^{-1}}$ [46]. The measured value for absorbance at 568 nm, $A_{568} = 0.095576$ is then introduced in equation 6, along with an optical path $l = 10^{-2}$cm and $\varepsilon_{M,568} = 6{,}3\times10^4\ \mathrm{M^{-1}cm^{-1}}$ yielding a molar density of c = 151,71 µM $(151.71\times10^{-6}\ \mathrm{mol/m^3})$. Multiplying this value by bR's molecular weight we get a concentration value in g L^{-1} of 3,945 or $3{,}945\times10^{-3}$ g mL^{-1}. Since the solution was later diluted 10-fold in buffer solution at deposition stage, in order to give the protein enough time to assemble itself favourably on the gold substrate and avoiding aggregation, the optimal molar density in the 10-20 µM range is achieved.

5.4 Absorption Spectroscopy on 247Cys bR on Gold Substrate

Raw transmittance (%T) acquired data is shown below in figure 5.6 for bare gold film (green), directly attached bR on gold (blue) and bR attached on thiolized gold (purple).

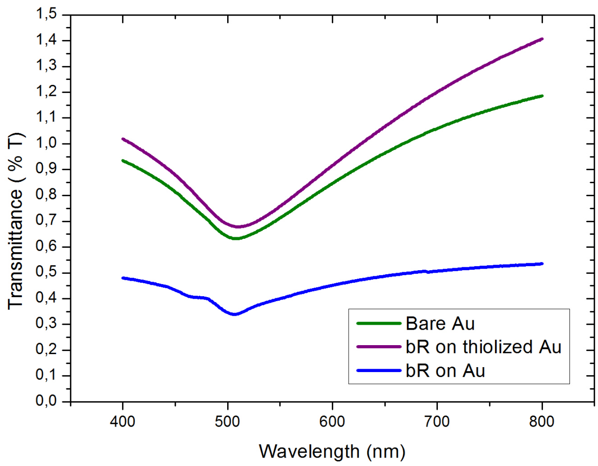

Figure 5.6 – Raw transmittance data spectra for plain gold, bR on gold and bR on thiolized gold.

Experimental baseline correction measurements were then subtracted to the raw data and transmittance is converted to absorbance through equation 3, resulting in the measured absorbance spectra presented in figure 5.7.

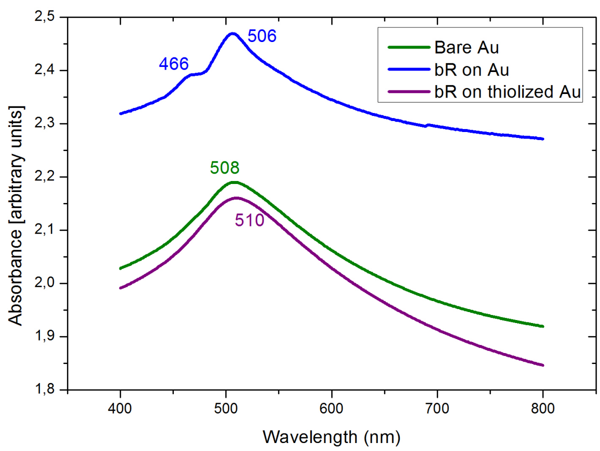

Figure 5.7 – Absorbance spectra for plain gold, bR on gold and bR on thiolized gold

Bare gold reveals absorption maximum at 508 nm, in accordance with literature for gold thin films [47]. bR directly attached to gold reveals a “blue” shift towards 506 nm and bR attached to thiolized gold revealed a “blue” shift towards 510 nm, both relative to bR absorption in solution. This is consistent with bR cysteine covalent attachment on gold with preservation of photocapabilities as reported in supporting information from literature [34]. Direct attachment also revealed a smaller peak at 466 nm, which may be indication of photocycle intermediate I_{460} formation. This would require measurement repetition for explanation.

Plotting deposited bR absorption on both gold substrates (bare and thiolized) against suspension absorption (rather than to bare gold chip) would result in interesting shift analysis due to attachment on gold.

The intrinsic background for each spectrum is then subtracted by using a horizontal baseline relative to each one of them after normalization at same background on the shortest wavelength site, in order to gain information on the relative intensities instead of their absolute value (Fig. 5.8). Peak positions are not affected by this procedure.

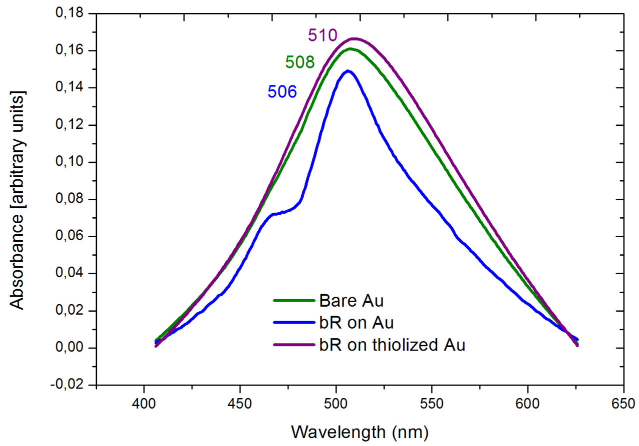

Figure 5.8 – Absorbance spectra with subtracted baselines. Relative absorption intensities are more clearly depicted.

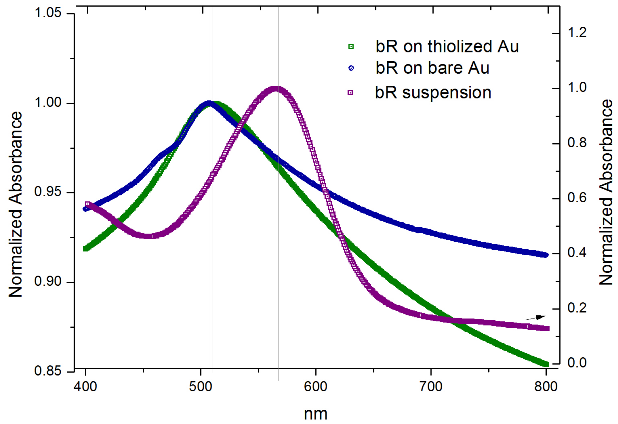

Figure 5.9 – Absorption peak shift to 510 nm upon bR deposition on gold substrate indicating covalent binding to substrate.

5.5 Atomic Force Microscopy Analysis

Height distribution function in the acquired AFM images, ρ, is computed through one-dimensional statistical analysis. Its values are determined by the software from normalized histograms of linear densities ρ (counts per nm) and its normalization is such that:

$$\int_{-\infty}^{+\infty} \rho(z)dz = 1$$

Height distribution in terms of total counts can be determined by multiplying the linear density ρ (nm^{-1}) by the total length of the AFM image (given by the number of lines multiplied by length of each line in nm).

5.5.1 Purple membrane deposition on mica

- **Bare mica**

Purple membrane deposition on bare mica (Fig. 5.10) reveals a highly covered surface, with high density and amount of deposited material. Any resolved structure in the topographic image should be due to deposited protein since mica sheets are assumed to be atomically flat.

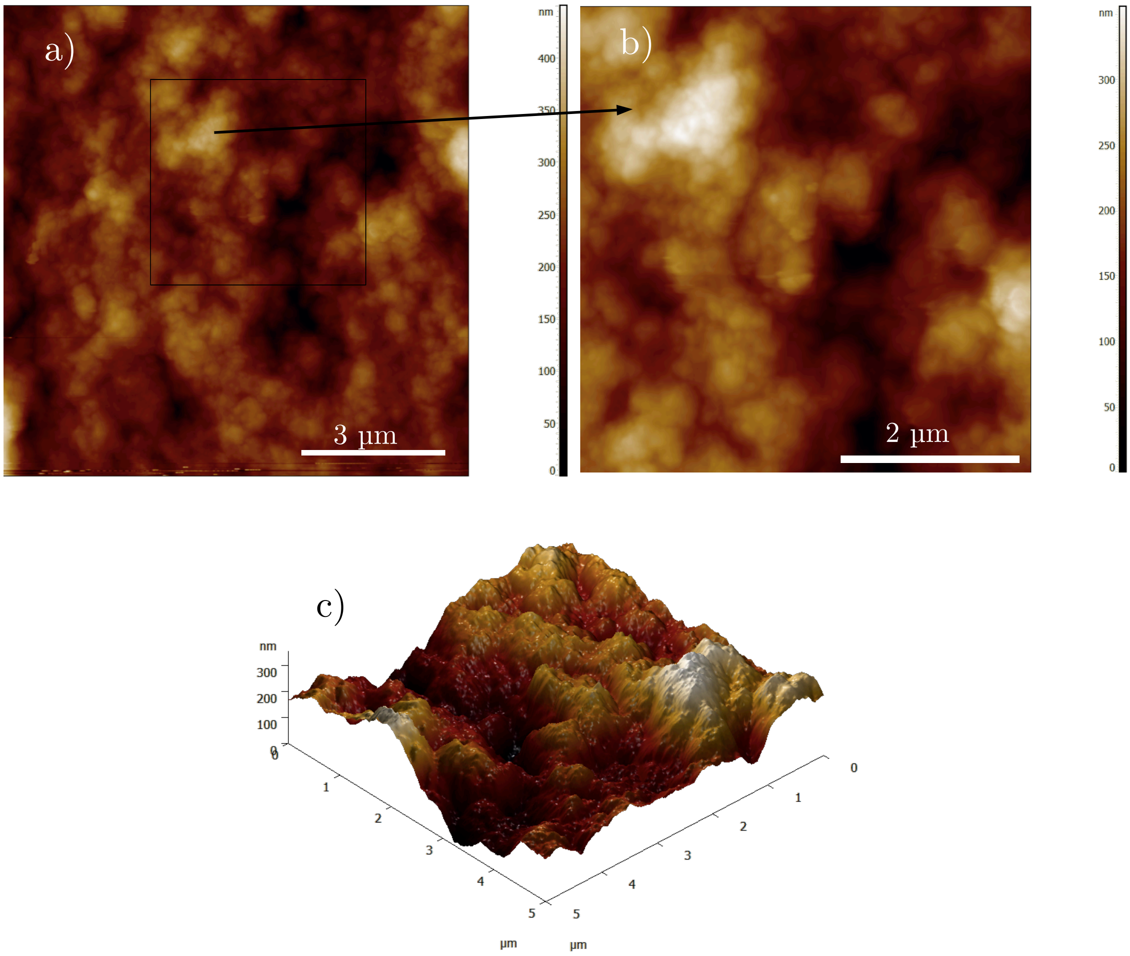

Figure 5.10 – Atomic Force Microscopy topographic images of PM directly deposited on mica. (a) 10x10 µm scan with vertical colour scale to the right. (b) 5x5 µm zoom from image a) with emphasis on vertically striking patch and vertical colour scale to the right. (c) 3D representation of image b).

Height distribution analysis (Fig. 5.11) from the entire 10x10 µm AFM image (Fig. 5.10a) reveals heights up to 656.2 nm with the most probable height (peak) at around (276 ± 162) nm. In terms of counts, for example, structures with 350 nm height, for which the height density is 0.0025/nm, represent about 13 000 counts in all AFM image.

However, knowing the nominal height of PM in native membrane is around 4-6 nm [8] and considering the high and broad determined height distribution (with values up to 100 times higher than PM in membrane), we are lead to the conclusion that multilayer deposition occurred, reflecting PM's aggregation and stacking tendency upon an uncontrolled deposition approach i.e. with no surface linker and no mutation to exploit preferential binding area, as referred in section 3.2.

- **Aminosilanized mica**

Aminosilanized mica topographic studies (Figure 5.12a) contrastingly reveal much sparser coverage and lower heights in relation to bare mica and also formation of visible patches protruding from a spotted plane, with areas spanning from a few hundreds to a thousand square nanometres. The three most prominent ones (A, B and C Fig. 5.12a) show maximum resolved heights between 12 and 25 nm and are expected due to PM's aggregation properties. Using height distribution analysis (Fig. 5.11 – green line), these prominent patches come across in the spectra as a component with a maximum at 17 nm and correspond to aproximately 0.6% of total area.

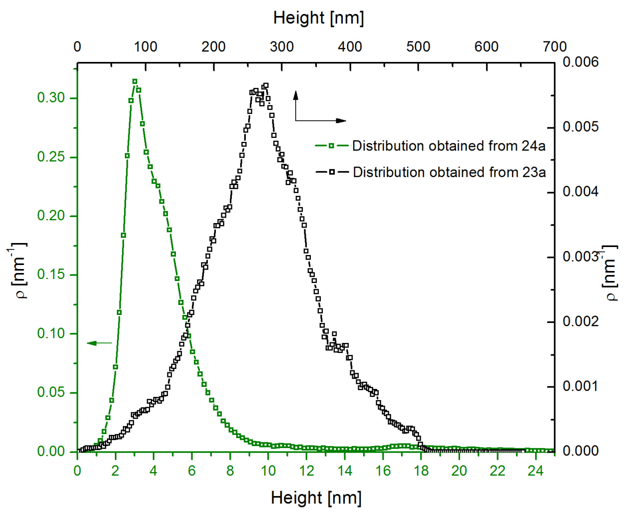

Figure 5.11 – Height distribution for PM deposition on mica substrate. Distribution from deposition on bare mica is represented in black and for deposition on aminosilanized mica in green.

Height distribution analysis (Fig. 5.11) from the entire 5x5 μm AFM image (Fig. 5.12a) reveals an overall most probable height (peak) of 3.05 nm with FWHM of 2.7 nm. However, with more thorough analysis, two main contributions in the distribution are visible: a narrower one centred in 3.01 nm with FWHM 1.03 nm and a wider one centered around 4.4 nm with FWHM 2.5 nm.

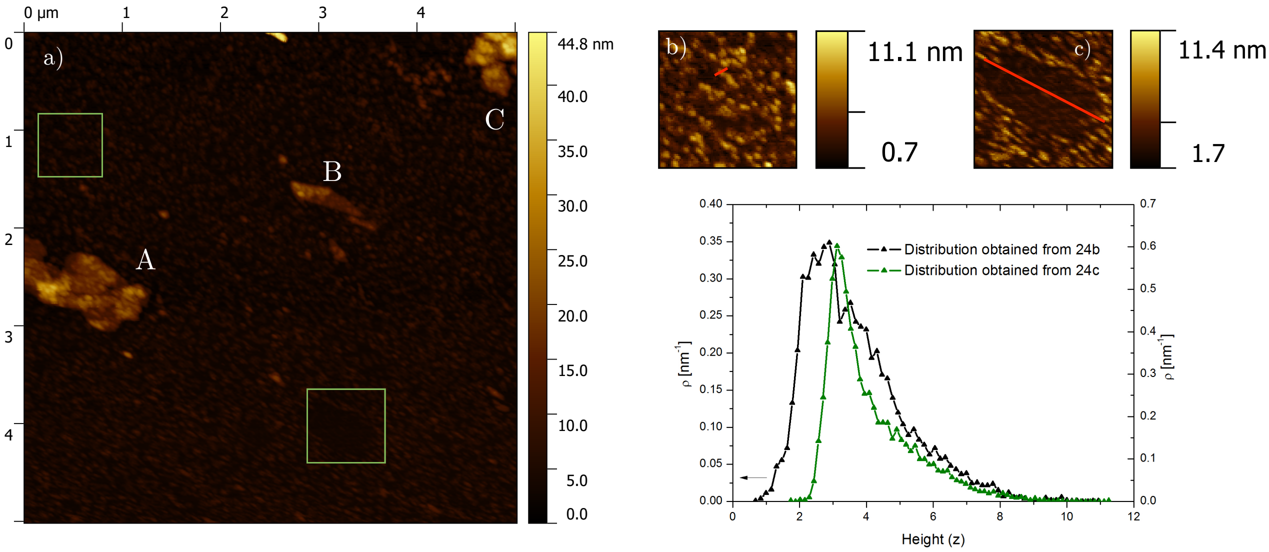

Figure 5.12 – Atomic Force Microscopy topographic images from sample 1 of PM deposited on aminosilanized mica. (a) 5x5 µm scan with homogeneous section highlighted on top and scarce coverage section on the bottom. (b) Homogeneous and representative section with profile section selection in red (c) Scarce coverage section with profile section selection in red. (d) Height distributions for b) and c)

Cropping (Fig. 5.12b) the most apparently homogeneous and representative section of figure 5.12a and determining the respective local height distribution (Fig. 5.12d), also suggests there are two main contributing distributions, roughly estimated to be centered around 2.7 nm with FWHM of 1.7 nm and 3.7 nm with FWHM of 1.9 nm. Here the two contributions come across more clearly in the shape of the distribution, and is in line with what was described above for the totality of the 5x5 µm image (Fig. 5.12a). Resolving one individual entity from the homogeneous section is possible though profile analysis (Fig. 5.13a) The feature is resolvable with approximately 4.96 nm high upon an unresolved 2 nm base and has a FWHM of around 48 nm.

Cropping another small section in the highlighted area of figure 5.12a where coverage appears scarce (Fig. 5.12c) allows for better understanding of lower height contribution in height distribution of the whole 5x5 µm image. Local height distribution is represented also in Figure 5.12d. It shows a more prominent contribution centred around 3.2 nm with FWHM of 0.8 nm and a much smaller one at 4.5 nm with FWHM of 2.2 nm, which can be refered to as background and assigned to trimeric bacteriorhodopsin units, respectively. bR nominal height of 4-6 nm is consistent with height os resolved structures and indicates that bR attached itself vertically due to electrostatic interaction between its most electronegative termini with positive silane

SAM. In order to check the backgroung effect on the height of the resolved structures, a section profile from figure 5.12c is shown (Fig. 5.13b), confirming the existence of two major contributions, one due to this background and another for resolvable trimeric entities, on top of said background.

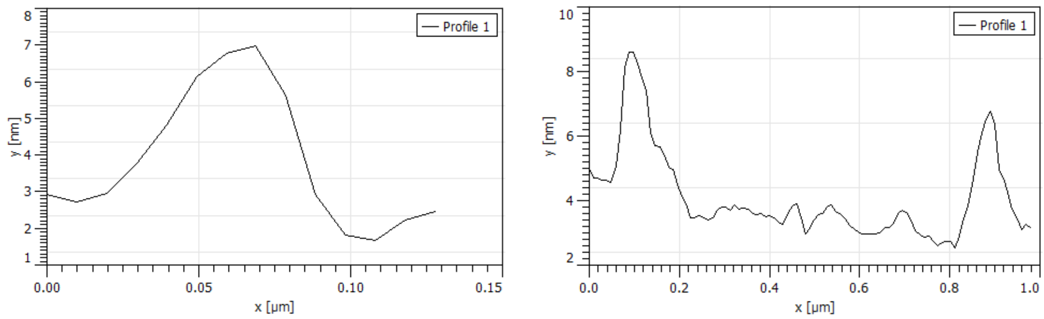

Figure 5.13 – (a) Profile of highlighted resolved structure from figure 5.11b. (b) Profile of selected section in figure 5.11c where background is apparent.

Contact angles of silane of 40° discussed in section 3.2, would make bR attach on silane and reveal itself in AFM with lower heights (around sin(40)×height), yielding heights of about 3.2 nm which we can, in first approximation, atribute as being responsible for the evident "background". A thick silane layer can also contibute to the nature of the background. Since APTES is a 7Å long molecule, a background with 3.2 nm heigh could indicate a 4-5 APTES molecule stacking.

The above described AFM analysis is consistent with a surface where PM adsorbed on mica in a more controlled way comparing to deposition on bare mica, which is indication that our deposition approach seems promising regarding controlled coverage and monolayer thickness.

5.5.2 **247Cys bR deposition on gold**

- **Bare gold**

AFM imaging of isolated 247Cys bR deposited on bare gold (Fig. 5.14) displays very high and homogeneous surface coverage with uniformly sized entities. Similar coverage results from Patil et. al. were refereed to as unprecedented. Significant patch absence is expected since 247Cys bR is released from PM structural lipids, and is confirmed in the acquired images.

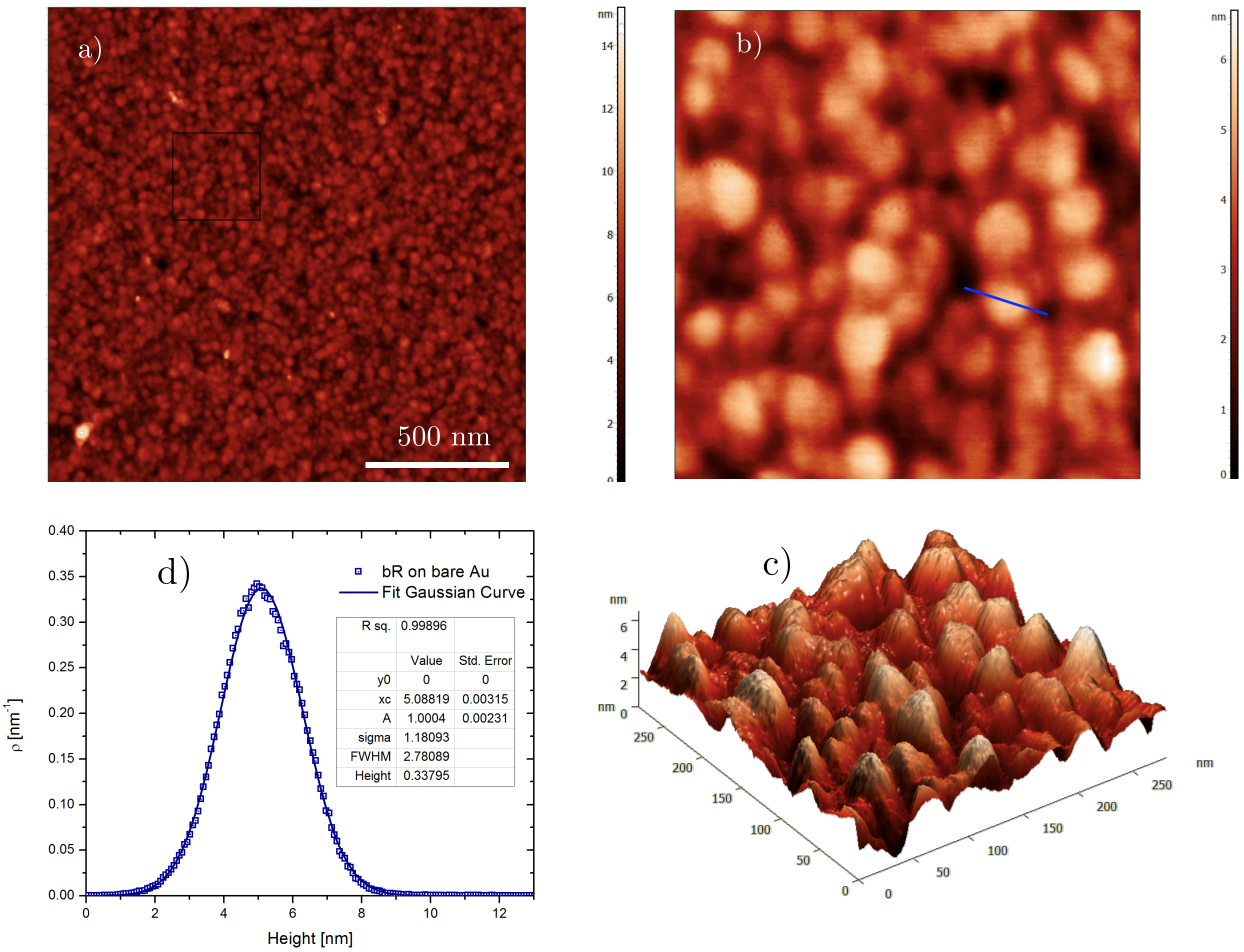

Figure 5.14 – AFM topographic images of 247Cys bR deposited on plain gold surface. (a) 1,5x1,5 µm scan. (b) 280x280 nm zoom from highlighted area from a) with structure profile selection in blue. (c) 3D representation of image b). (d) Height distribution for whole 1,5x1,5 µm image.

Height distribution analysis for figure 5.14a (Fig. 5.14d) reveals a single peak with uniform distribution, further confirmed by mathematical Gaussian fitting. The highly satisfactory fit ($R^2 = 0.99896$ and integral area of 1.0004, in accordance with above mentioned normalization for height density) returns a Gaussian curve centred around 5.088 nm with FWHM of 2.781 nm.

The centre of the distribution matches that of bR's trimeric height and suggests the resolved features in the AFM image are assigned to individual bR trimers. This is further confirmed by profile section analysis of resolved entities. Profile from selected section in figure 5.14b (Fig. 5.15) allows measuring of a resolvable height of 5.006 with a FWHM of 31.9 nm. These dimensions are consistent with bR trimer diameter of 30-40 nm and height of 4-6 nm mentioned throughout literature.

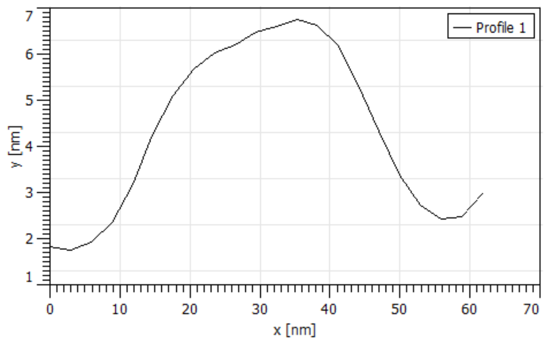

Figure 5.15 Profile of highlighted resolved structure from figure 5.14b.

It is safe to conclude from the AFM images that bR trimers have attached vertically to the Au substrate thus confirming good approach for high orientation control and layer thickness upon deposition. Homogeneous coverage and uniform entity size can be justified by well engineered bR anchoring mechanism via cystein mutation on the 247th residue, whose high affinity towards covalent bonding to gold atoms from surface dominates the possible interactions associated with the system, like non-specific Au-protein binding.

- **Thiolized gold**

When the 1,6-hexanedithiol surface linker is introduced for bR attachment on Au, three main planes are distinguishable in the AFM image (Fig. 5.16a): a base ascribed as background at around 1 nm, a dense intermediate one containing individual entities with resolved heights between 2 and 29 nm protruding from the base, and a third higher one containing structures higher than 30 nm (which comprise less than 1% of the total 5x5 µm area).

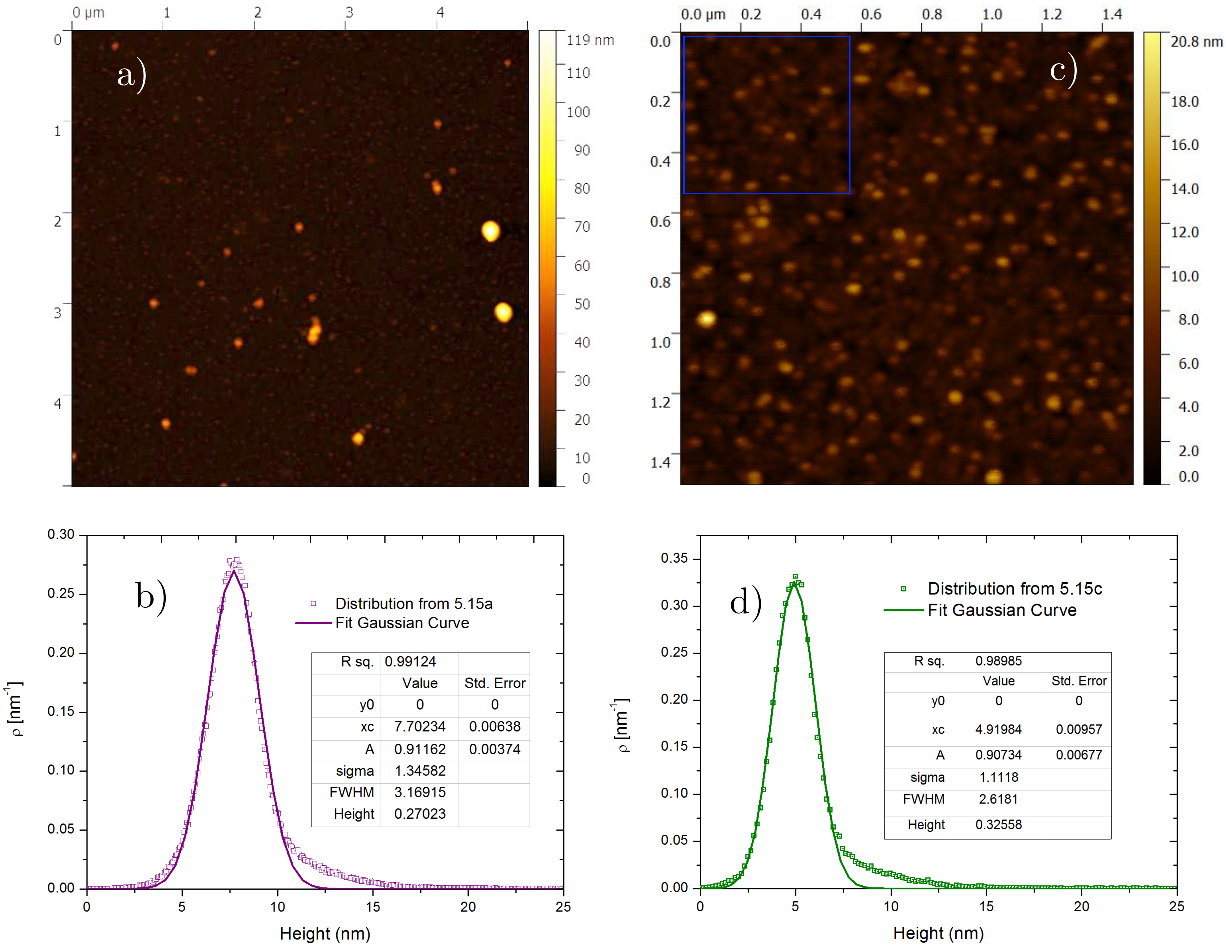

Figure 5.16 – AFM topographic images of 247Cys bR deposited on thiolized gold surface. (a) 5x5 µm scan. (b) Height distribution spectra for a). (c) 1.5x1.5 µm scan. (d) Height distribution spectra for c).

Determining height distribution spectra (Fig. 5.16b) for the above-mentioned image and fitting a Gaussian curve to the data, yields a distribution centred around 7.702 nm with a FWHM of 3.169 nm, 2.614 nm above the centre of distribution for deposition on bare gold. Still, these values are coherent with bR attachment. The fitted curve integral is 0.91162, below the value (induced from normalization) of 1, which is visible at the peak but more significantly at the right-side tail where fitting underestimates counts for structures with heights bigger than 10 nm. This may indicate that 1,6-hexanedithiol chain formation between sulphur atoms of dithiols anchored bR trimers at bigger heights.

Acquiring a more homogeneous and representative 1.5x1.5 µm section (Fig. 5.16c), where less contribution from features with height over 20 nm, and determining its local height distribution (Fig. 5.16d), shows that it lacks the uniformity achieved for deposition on bare gold (and reflected on accurate Gaussian fit) and this comes across in the distribution spectra in the form of a "tail" on the right side of the main peak. This means the heights of resolved structures are more disperse towards superior values.

Upon Gaussian fitting for the height distribution data, the obtained curve is centred around 4.920 nm with FWHM of 2.618 nm, more consistent with the results obtained for bare Au (only 3.3% lower) and can be assigned to bR trimeric entities. Its integral area is lower than that imposed by normalization due to right-tail underestimation for heights bigger than 7 nm. In relation to the whole 5x5 µm image distribution, the fitted curve shifted 2.782 nm towards lower heights and became narrower, consistent with more homogeneity in the section.

Cropping a sector from the 1.5x1.5 µm image (Fig. 5.17a) and analysing the highlighted profile section (Fig. 5.17b) one can depict a dark 2 nm background from which a 5.96 nm high structure protrudes, with FWHM of 27.2 nm. Again, these dimensions are in accordance with bR height and so, these resolved structures can be assigned to individual bR trimeric entities.

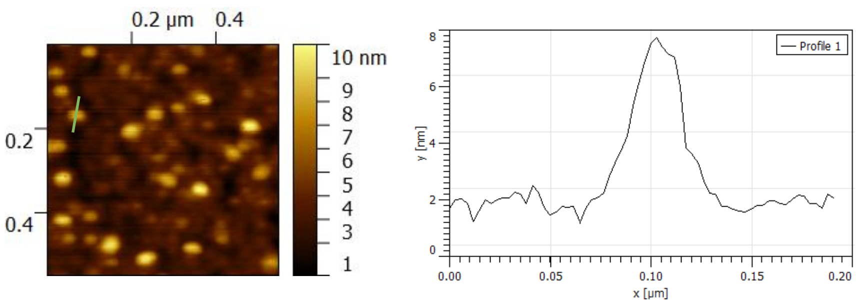

Figure 5.17 – (a) 500x500 nm section from 5.15c with profile selection in green. (b) profile of resolved structure.

6 Conclusions and Future Perspectives

AFM imaging of bR deposited on mica substrates allowed for comprehension of surface linker impact upon deposition. Clearly the layer volume decreased significantly and better control was achieved by imposing a positive surface charge for the most electronegative termini of bR to attach. Also, orientation is achieved and confirmed by the height distribution analysis made for these samples. Electrostatic forces should allow bacteriorhodopsin to preserve its native photodynamics since structure rearrangement is permitted.

Introducing a surface reactive cysteine residue and releasing bR trimers from its native lipid membrane structure results in unpatched highly oriented monolayer bR films, uniformly and robustly immobilized through covalent attachment, the strongest chemical bond. Introducing a surface linker on a gold surface best preserves bR's photoelectrical properties for nanobiodevice application and should result in enhanced generated photocurrent through direct electron transfer mechanisms. In order to confirm this, photoelectric response studies and IV curve analysis can elucidate how the thiol monolayer affects bR's photodynamics. Also, regarding deposition uniformity and unspecific interactions, XPS studies would result in interesting information on how to optimize bR's binding to the surface linker by minimizing thiol loops.

247Cys bR is a very attractive candidate for photoelectric biomedical applications since orientation control and deposited layer thickness results were better in relation to the self-assembled layering achieved with native purple membrane on mica substrates. Further absorption enhancement via gold nanoparticle field-effect enhancement, achieve higher efficiencies than conventional silicon-based technologies. Sub retinal implants rely on a photoactive amplification stage in order to be able to stimulate remainder healthy tissue, and specifically mimics PM quaternary structure lattice for optimization. PM dynamics studies can be performed in order to better understand the stabilizing effects of crystallographic and membrane lipids in bR's photocycle.

The amazing properties of bacteriorhodopsin, more than being considered for photoelectric applications, can also impact cell radiologic protection studies in the way that proton translocation through membrane is a natural cell mechanism that could be enhanced by molecular dynamic studies of bR's conformation changes through time.

This work involved some challenges, especially since all the material and instrumentation were based in Aalborg, disabling systematic studies and diminishing chances for further investigation via other experimental methods.

The present work has also had a great impact on the author's academic path, having ignited an intellectual spark towards the study of this remarkable protein and relation to nanotechnological nature mimicry. The possibilities are immense and extremely promising regarding biomedical research.

References

[1] W. Kühlbrandt, “Bacteriorhodopsin - the movie.,” *Nature*, vol. 406, no. August, pp. 569–570, 2000.

[2] R. R. Birge, “Protein-Based Optical Computing and Memories,” *Computer (Long. Beach. Calif).*, vol. 25, no. 11, pp. 56–67, 1992.

[3] C. Nicolini, V. Erokhin, S. Paddeu, and M. Sartore, “Towards a light-addressable transducer bacteriorhodopsin based,” *Nanotechnology*, vol. 9, no. 3, pp. 223–227, 1999.

[4] W. Stoeckenius and R. Rowen, “A morphological study of Halobacterium halobium and its lysis in media of low salt concentration.,” *J. Cell Biol.*, vol. 34, no. 1, pp. 365–393, 1967.

[5] M. Montal, “Electrical demonstration of rapid light-induced conformational changes in bacteriorhodopsin,” *Nature*, vol. 267, p. 673, 1977.

[6] Y. Jin, N. Friedman, M. Sheves, T. He, and D. Cahen, “Bacteriorhodopsin (bR) as an electronic conduction medium: current transport through bR-containing monolayers.,” *Proc. Natl. Acad. Sci. U. S. A.*, vol. 103, no. 23, pp. 8601–8606, 2006.

[7] N. Hampp and D. Oesterhelt, “Bacteriorhodopsin and its potential in technical applications,” *Nanobiotechnology*, pp. 146–167, 2005.

[8] N. A. Hampp, “Bacteriorhodopsin: mutating a biomaterial into an optoelectronic material,” *Appl Microbiol Biotechnol*, vol. 53, no. 6, pp. 633–639, 2000.

[9] B. Y. Chow, X. Han, A. S. Dobry, X. Qian, A. S. Chuong, M. Li, M. A. Henninger, G. M. Belfort, Y. Lin, P. E. Monahan, and E. S. Boyden, “High-performance genetically targetable optical neural silencing by light-driven proton pumps.,” *Nature*, vol. 463, no. 7277, pp. 98–102, 2010.

[10] V. Gradinaru, F. Zhang, C. Ramakrishnan, J. Mattis, R. Prakash, I. Diester, I. Goshen, K. R. Thompson, and K. Deisseroth, “Molecular and

Cellular Approaches for Diversifying and Extending Optogenetics," *Cell*, vol. 141, no. 1, pp. 154–165, 2010.

[11] N. L. Wagner, J. a Greco, M. J. Ranaghan, and R. R. Birge, "Directed evolution of bacteriorhodopsin for applications in bioelectronics.," *J. R. Soc. Interface*, vol. 10, no. 84, p. 20130197, 2013.

[12] M. Frydrych, P. Silfsten, S. Parkkinen, J. Parkkinen, and T. Jaaskelainen, "Color sensitive retina based on bacteriorhodopsin," *BioSystems*, vol. 54, no. 3, pp. 131–140, 2000.

[13] W. W. Wang, G. K. Knopf, and A. S. Bassi, "Bioelectronic imaging array based on bacteriorhodopsin film," *IEEE Trans. Nanobioscience*, vol. 7, no. 4, pp. 249–256, 2008.

[14] C. S. Yelleswarapu, S. R. Kothapalli, and D. V. G. L. N. Rao, "Optical Fourier techniques for medical image processing and phase contrast imaging," *Opt. Commun.*, vol. 281, no. 7, pp. 1876–1888, 2008.

[15] S. R. Kothapalli, P. Wu, C. S. Yelleswarapu, and D. V. G. L. N. Rao, "Medical image processing using transient Fourier holography in bacteriorhodopsin films," *Appl. Phys. Lett.*, vol. 85, no. 24, pp. 5836–5838, 2004.

[16] B. Mahyad, S. Janfaza, and E. Sadat, "Bio-nano hybrid materials based on bacteriorhodopsin : Potential applications and future strategies," *Adv. Colloid Interface Sci.*, vol. 225, pp. 194–202, 2015.

[17] P. Saeedi, J. M. Moosaabadi, S. S. Sebtahmadi, J. F. Mehrabadi, M. Behmanesh, and S. Mekhilef, "Potential applications of bacteriorhodopsin mutants," *Bioengineered*, vol. 3, no. 6, pp. 326–328, 2012.

[18] S. Trivedi, O. P. Choudhary, and J. Gharu, "Different proposed applications of bacteriorhodopsin.," *Recent Pat. DNA Gene Seq.*, vol. 5, no. 1, pp. 35–40, 2011.

[19] A. V. Patil, T. Premaruban, O. Berthoumieu, A. Watts, and J. J. Davis, "Enhanced photocurrent in engineered bacteriorhodopsin monolayer," *J. Phys. Chem. B*, vol. 116, pp. 683–689, 2012.

[20] K. Barrett, H. Brooks, S. Boitano, and S. Barman, "Chapter 12: Vision," in *Ganong's Review of Medical Physiology*, 2010, pp. 181–201.

[21] P. Garriga and J. Manyosa, "The eye photoreceptor protein rhodopsin. Structural implications for retinal disease," *FEBS Lett.*, vol. 528, no. 1–3, pp. 17–22, 2002.

[22] E. Zrenner, "Artificial vision: Solar cells for the blind," *Nat. Photonics*, vol. 6, no. 6, pp. 344–345, 2012.

[23] H. G. Choi, W. C. Jung, J. Min, W. H. Lee, and J. W. Choi, "Color image detection by biomolecular photoreceptor using bacteriorhodopsin-based complex LB films," *Biosens. Bioelectron.*, vol. 16, no. 9–12, pp. 925–935, 2001.

[24] R. Neutze, E. Pebay-Peyroula, K. Edman, A. Royant, J. Navarro, and E. M. Landau, "Bacteriorhodopsin: A high-resolution structural view of vectorial proton transport," *Biochim. Biophys. Acta - Biomembr.*, vol. 1565, no. 2, pp. 144–167, 2002.

[25] K. Voïtchovsky, "Atomic Force Microscopy and Force Spectroscopy of Biomembranes and Applications to Nanotechnology," 2006.

[26] C. H. Martin, Z. P. Chen, and R. R. Birge, "Towards a bacteriorhodopsin-silicon neuromorphic photosensor.," *Pac. Symp. Biocomput.*, pp. 268–79, 1997.

[27] H. G. Khorana, "Bacteriorhodopsin, a membrane protein that uses light to translocate protons.," *J. Biol. Chem.*, vol. 263, no. 16, pp. 7439–7442, 1988.

[28] U. Haupts, J. Tittor, and D. Oesterhelt, "Closing in on bacteriorhodopsin: progress in understanding the molecule.," *Annu. Rev. Biophys. Biomol. Struct.*, vol. 28, pp. 367–399, 1999.

[29] H. Luecke, B. Schobert, H. T. Richter, J. P. Cartailler, and J. K. Lanyi, "Structure of bacteriorhodopsin at 1.55 A resolution.," *J. Mol. Biol.*, vol. 291, pp. 899–911, 1999.

[30] K. M. Al-Aribe, G. K. Knopf, and A. S. Bassi, "Photoelectric monolayers based on self-assembled and oriented purple membrane patches," *J. Microelectromechanical Syst.*, vol. 20, no. 4, pp. 800–810, 2011.

[31] A. Aharoni, B. Hou, N. Friedman, M. Ottolenghi, I. Rousso, S. Ruhman, M. Sheves, T. Ye, and Q. Zhong, "NonnIsomerizable Artificial Pigments: Implications for the Primary LighttInduced Events in Bacteriorhodopsin," *Biochem. Transl. from Biokhimiya Orig. Russ. Text*, vol. 66, no. 11, pp. 121001219–149991510, 2001.

[32] B. Schmidt, C. Sobotta, B. Heinz, S. Laimgruber, M. Braun, and P. Gilch, "Excited-state dynamics of bacteriorhodopsin probed by broadband femtosecond fluorescence spectroscopy," *Biochim. Biophys. Acta - Bioenerg.*, vol. 1706, no. 1–2, pp. 165–173, 2005.

[33] Y. Jin, N. Friedman, M. Sheves, and D. Cahen, "Bacteriorhodopsin-monolayer-based planar metal-insulator-metal junctions via biomimetic vesicle fusion: preparation, characterization, and bio-optoelectronic characteristics," *Adv. Funct. Mater.*, vol. 17, no. 8, pp. 1417–1428, 2007.

[34] O. Berthoumieu, A. V. Patil, W. Xi, L. Aslimovska, J. J. Davis, and A.

Watts, “Molecular scale conductance photoswitching in engineered bacteriorhodopsin,” *Nano Lett.*, vol. 12, pp. 899–903, 2012.

[35] a Mahmoudzadeh, R. Saer, D. Jun, S. M. Mirvakili, a Takshi, B. Iranpour, E. Ouellet, E. T. Lagally, J. D. W. Madden, and J. T. Beatty, “Photocurrent generation by direct electron transfer using photosynthetic reaction centres,” *Smart Mater. Struct.*, vol. 20, p. 94019, 2011.

[36] K. M. Al-Aribe, G. K. Knopf, and A. S. Bassi, “Organic photovoltaic cells based on photoactive bacteriorhodopsin proteins,” vol. 8615, p. 86150Q, 2013.

[37] A. Ulman, M. Ioffe, F. Patolsky, E. Haas, and D. Reuvenov, “Highly active engineered-enzyme oriented monolayers: formation, characterization and sensing applications.,” *J. Nanobiotechnology*, vol. 9, no. 1, p. 26, 2011.

[38] T. Y. B. Leung, M. C. Gerstenberg, D. J. Lavrich, G. Scoles, F. Schreiber, and G. E. Poirier, “1,6-Hexanedithiol monolayers on Au(111): A multitechnique structural study,” *Langmuir*, vol. 16, no. 2, pp. 549–561, 2000.

[39] H. J. Butt, K. H. Downing, and P. K. Hansma, “Imaging the membrane protein bacteriorhodopsin with the atomic force microscope.,” *Biophys. J.*, vol. 58, no. 6, pp. 1473–1480, 1990.

[40] A. R. Yadav, R. Sriram, J. A. Carter, and B. L. Miller, “Comparative study of solution–phase and vapor–phase deposition of aminosilanes on silicon dioxide surfaces,” *Mater. Sci. Eng. C*, vol. 35, no. 3, pp. 283–290, Feb. 2014.

[41] T. Verbiest, K. Clays, and V. Rodriguez, *Second-Order Nonlinear Optical Characterization Techniques An Introduction*. 2009.

[42] A. Abdul-gader, A. J. Miles, and B. A. Wallace, “A reference dataset for the analyses of membrane protein secondary structures and transmembrane residues using circular dichroism spectroscopy,” vol. 27, no. 12, pp. 1630–1636, 2011.

[43] B. Wallace, J. Lees, and A. Orry, “AWallace, B., Lees, J., & Orry, A. (2003). Analyses of circular dichroism spectra of membrane proteins. Protein ..., 875–884. doi:10.1110/ps.0229603.structuralnalyses of circular dichroism spectra of membrane proteins,” *Protein ...*, pp. 875–884, 2003.

[44] L. Whitmore and B. A. Wallace, “Protein secondary structure analyses from circular dichroism spectroscopy: Methods and reference databases,” *Biopolymers*, vol. 89, no. 5, pp. 392–400, 2008.

[45] Govindjee, J. Amesz, and D. D. Fork, “Light emission by plants and bacteria,” *J. Biolumin. Chemilumin.*, vol. 2, 1986.

[46] H. Vogel and W. Gärtner, "The secondary structure of bacteriorhodopsin determined by Raman and circular dichroism spectroscopy.," *J. Biol. Chem.*, vol. 262, no. 24, pp. 11464–11469, 1987.

[47] B. Abel, T. S. Kabir, B. Odukoya, M. Mohammed, and K. Aslan, "Enhancement of the colorimetric response of enzymatic reactions by thermally evaporated plasmonic thin films: application to glial fibrillary acidic protein," *Anal. Methods*, vol. 7, no. 3, pp. 1175–1185, 2015.